lajss.org
Latin American Journal of Solids and Structures
www.lajss.org

Numerical investigation on wind pressure mitigation in low-rise building roofs using spoilers with PID control

Gabriela Penna Bianchin 1[a*] https://orcid.org/0009-0004-6316-574X , Alexandre Luis Braun 2 [a] https://orcid.org/0000-0002-6170-3653

[a] Programa de Pós-Graduação em Engenharia Civil, Universidade Federal do Rio Grande do Sul – PPGEC/UFRGS, Porto Alegre, RS, Brasil. E-mail: pbianchingabi@gmail.com; alexandre.braun@ufrgs.br

* Corresponding author

Abstract

A numerical investigation is performed in this work to evaluate the influence of controlled spoilers on pressure mitigation over low-rise building roofs. Considering that low-rise buildings are susceptible to severe damages caused by wind action, spoilers are utilized along the roof windward edges to reduce the aerodynamic load, which are controlled using PID control techniques. Numerical simulations are carried out using a semi-implicit Characteristic-based Split algorithm, where linear tetrahedral finite elements are employed for spatial discretization in a standard Galerkin procedure. Turbulence modeling is performed using Large Eddy Simulation and the flow fundamental equations are written considering isothermal and incompressible conditions in arbitrary Lagrangian-Eulerian kinematical description to consider the spoiler angular motion. Two and three-dimensional simulations are carried out using a low-rise building model, where the influence of controlled roof spoilers is evaluated. Wind tunnel predictions are utilized to validate the numerical formulation proposed here.

Keywords

Low-rise buildings, Pressure mitigation, PID control, Large Eddy Simulation (LES), Finite Element Method (FEM), Computer Fluid Dynamics (CFD)

1 INTRODUCTION

Low-rise building roofs are known to be susceptible to the wind action due to strong pressure loads developed over the roof surfaces, which are induced by flow separation occurring at roof sharp edges, such as eaves and ridges, especially under extreme climate events. It is also well known that the failure mechanism of structural and covering elements localized in the roof are intimately related to load resultants obtained from the combination of inner and outer pressure conditions, where wall openings play a major role (see, for instance, Blessmann, 2009). Among several pressure mitigation devices available, spoilers can be utilized along the roof lateral edges to suppress the formation of large vortices in that region (Li et al., 2018).

Low-rise buildings are enclosed structures with less than 15 m in height (Holmes, 2015) and usually submitted to atmospheric boundary layer flows, where turbulence effects may be significant. The roof structure design is critical in this case, considering that high suction pressures are developed over covering elements located near sharp edges of the roof. Negative pressures are produced due to flow separation along the windward edges and the worst situation occurs when wind flows with oblique directions are observed, leading to extreme suctions that result from conical vortices forming at roof corners (Banks et al., 2000). One can see that the vortex formation mechanism at the ridges and eaves of gable roof buildings is different from that of flat roof buildings (Prasad et al., 2009).

The roof structure is usually submitted to higher aerodynamic loads than those observed in any other building element. Consequently, roof covering elements such as shingles, tiles and pavers are considered as the most vulnerable part of a low-rise building, especially during wind storms, when loose roofing components may be dislodged, becoming a source of wind-borne debris. Once part of the roof has failed, a sequence of structural failures is triggered: breaches on the roof surface lead to adverse internal pressures, increasing the aerodynamic loads on the roof, doors and windows. With the break of the building envelope, internal pressurization is observed, which could cause additional structural failures (Huang et al., 2014). Owing to improvements obtained in building codes over the last decades, failures in the building structural system are scarce, but severe damages are still inflicted to the building envelope by the wind-induced forces.

The aerodynamic loading on the roof structure can be significantly modified if the permeability due to openings in the building walls is taken into account, which may induce positive pressures on the inner roof surface depending on the opening distribution over the building facades (Blessmann, 2013). This pressure combination is mainly observed in low-rise industrial buildings and sports halls or gymnasia, where inner and outer flow environments interact.

Mitigation strategies have been developed over the last decades in order to reduce the aerodynamic loading on low-rise building roofs by modifying roof corners and edges or including aerodynamic appendices to attenuate high negative pressures produced by conical vortices (see, for instance, Surry and Lin, 1995; Kopp et al., 200; Bitsuamlak et al., 2013; Huang et al., 2014; Mooneghi and Kargarmoakhar, 2016). The mitigation techniques proposed so far may be classified into two approaches: roof geometric modification and disturber installation. Roof geometric modification refers to minor changes in the shape of roof corners and edges to modify the flow pattern on the roof surface and reduce suction pressures. On the other hand, a disturber is utilized to reduce negative pressures by disrupting the vortex formation and deflecting the conical vortices from the roof surface, which are the main responsible for extreme roof suctions. Disturbers have been mainly utilized in the form of parapets with different shapes and configurations or passive aerodynamic edges. The aerodynamic mitigation techniques are based on shape modification to improve the aerodynamic behavior of building roofs. In this context, curved and chamfered edges have been proposed to reduce aerodynamic loads on gable-roof buildings. Robertson (1991) evaluated the effectiveness of different roof eave configurations on the wind load mitigation using full-scale measurements and Surry and Lin (1995) investigated the sensitivity of high suctions to some minor modifications in the roof corner geometries. The high wind-induced suctions occurring at roofs and wall corners were found to be reduced through the use of simple architectural elements in Bitsuamlak et al. (2013), while Huang et al. (2014) experimentally assessed the effects of typical eaves and gutters on mitigating the critical wind effects over low-rise building roofs. In general, corner modifications have not obtained significant reductions in terms of roof uplift forces (Aly and Bresowar, 2016), although they have been effectively utilized as a mitigation technique for tall buildings (see, for instance, aAlminhana et al., 2018; bAlminhana et al., 2018), as pointed out previously by Kareem et al. (1999).

Parapets have been considered and extensively utilized as a mitigation device for flat-roof buildings, which can deviate the separated shear layers from the roof surface, leading to dissipation of local high suctions over wide areas. Baskaran and Stathopoulos (1988) are one of the first authors to investigate the influence of building roof parapets on the vortex suppression mechanism, who demonstrated that high parapets can reduce high suctions at roof corners generally, but low parapets may lead to increments in the aerodynamic load on interior regions (see also, Wu, 2000). In addition, parapets are usually submitted to high aerodynamic forces, such that drawbacks associated with its use may

surpass the benefits. The effectiveness of different parapet configurations and positions on roof pressure mitigation were also investigated by Surry and Lin (1995), Pindado and Meseguer (2003), Suaris and Irwin (2010) and Kopp et al. (2005), who systematically evaluated the aerodynamic performance of various parapets by using wind tunnel experiments, which included continuous, partial and porous parapets, as well as fences and spoilers. Results demonstrated that spoilers and porous continuous parapets obtained the best performances.

Banks (2000) carried out wind tunnel tests using different mitigation methods for reducing suction pressures associated with separated flows, which included a mounted spoiler. Results demonstrated that vortex spoilers obtained a better mitigation response than those observed using other devices. A similar conclusion was obtained by Aly and Bresowar (2016), who presented a comparative study on aerodynamic mitigation devices for low-rise building roofs. Li et al. (2018) investigated the wind pressure mitigation effect on the roof of a low-rise gable-roof building with spoilers using wind tunnel experiments. The experimental predictions showed the maximum pressure mitigation is obtained when spoilers are located at the gable, followed by spoilers located at the eave. When a spoiler was located at the ridge, no noticeable decrease was observed in terms of wind-induced pressures on the roof. Spoilers were also utilized by Banks et al. (2001) and Kopp et al. (2005) as a mitigation device for attenuation of negative pressures on low-rise building roofs. Although some investigations on pressure mitigation in low-rise building roofs have been proposed using spoilers, it is important to notice that all these works were carried out considering that the mitigation devices were fixed.

Control surfaces have been adopted to suppress aeroelastic instabilities and reduce aerodynamic loads due to wind action on tall buildings and long-span bridges (see, for instance, Sangalli and Braun, 2020), where passive or controlled devices are utilized. These aerodynamic appendices can also be designed to reduce the wind loading on low-rise building roofs, which may be automatically adjusted according to instantaneous flow conditions, similar to flight devices utilized in airplane wings, such as spoilers and slats. In this sense, PID control techniques could be employed to determine the orientation of spoilers attached to the roof edges in order to attenuate wind loads on the roof structure. Nevertheless, to the authors' knowledge, no pressure mitigation method using control techniques has been proposed so far for reducing aerodynamic loads on low-rise building roofs. Details on PID controllers may be obtained in Aström and Hägglund (1995) and Aström and Hägglund (2005).

In the present work, a pressure mitigation device is proposed to alleviate the wind load on building roofs, where spoilers with PID control are utilized along the roof lateral edges. The influence of controlled spoilers on the wind load over the roof surface is evaluated considering building models with and without openings in the lateral walls. A finite element model based on the semi-implicit CBS scheme is utilized, where linear tetrahedral elements are adopted for spatial discretization. The flow fundamental equations are written using an Arbitrary Lagrangian-Eulerian (ALE) kinematical description, where Large Eddy Simulation (LES) is adopted for turbulence modeling. A mesh motion scheme is employed to accommodate spoiler motions within the flow spatial field. Two-dimensional preliminary simulations are performed considering a typical low-rise building model in order to calibrate the control formulation for spoilers located at the roof windward edge, where the influence of wall openings on the roof loading is also considered. The numerical formulation proposed here is validated using three-dimensional simulations based on wind tunnel tests referring to a low-rise industrial building model.

2 FLOW EQUATIONS

Some physical assumptions concerning the fluid flow modeling adopted here are initially presented. In the field of Computational Wind Engineering – CWE, wind flows are usually characterized with the following hypotheses (see aBraun and Awruch, 2009):

(1) Natural wind streams are considered to be within the incompressible flow range.

(2) Natural wind streams are considered to be within the turbulent flow range.

(3) Wind is constantly flowing with a constant temperature (isothermal process).

(4) Gravity forces are neglected in the flow field.

(5) Air is considered mechanically as a Newtonian fluid.

Consequently, the flow fundamental equations are reduced to the well-known Navier-Stokes and continuity equations (see White, 2005). These equations are written here using an ALE kinematical description to consider the presence of moving bodies immersed in the flow field. Flow turbulence is resolved using LES and Smagorinsky subgrid-scale modeling (Smagorinsky, 1963; Germano et al., 1991; Lilly, 1992).

The system of flow fundamental equations may be written as follows:

$$\frac{\partial v_i}{\partial t} + (v_j - w_j)\frac{\partial v_i}{\partial x_j} = \frac{1}{\rho}\frac{\partial}{\partial x_j}(\sigma_{ij} + \tau_{ij}^{SGS}) \qquad (i, j = 1,2,3) \qquad \text{in } \Omega^{\mathrm{f}} \tag{1}$$

$$\frac{\partial v_i}{\partial x_i} = 0 \qquad (i = 1,2,3) \qquad \text{in } \Omega^{\mathrm{f}} \tag{2}$$

where ρ is the fluid specific mass and xi are the components of the coordinate vector **x**, which is defined according to a three-dimensional rectangular Cartesian coordinate system. The velocity components vi and wi are related to the flow velocity vector **v** and mesh velocity vector **w**, respectively. The flow fundamental equations are valid in the flow spatial domain Ω^{f}, which is bounded by Γ_t^{Tf} at a time instant t, with t ∈ [0, T], where the subscript t indicates time dependence on the spatial domain during the time interval [0, T]. Notice that the flow velocities vi utilized in Eqs. (1) and (2) correspond to the large-scale component in a LES formulation.

The components of the fluid stress tensor **σ** are given according to the Newtonian constitutive model for viscous fluids, that is:

$$\sigma_{ij} = -p\delta_{ij} + \tau_{ij} \tag{3}$$

where *p* is the thermodynamic pressure, δ_{ij} are the components of the Kroenecker's delta (δ_{ij} = 1 for *i* = *j*; δ_{ij} = 0 for *i* ≠ *j*) and τ_{ij} are the components of the viscous stress tensor **τ**, which are expressed as:

$$\tau_{ij} = \mu\left(\frac{\partial v_i}{\partial x_j} + \frac{\partial v_j}{\partial x_i}\right) + \lambda\frac{\partial v_k}{\partial x_k}\delta_{ij} \qquad (i, j, k = 1,2,3) \tag{4}$$

where μ and λ are the dynamic and volumetric viscosities of the fluid. For incompressible flows, it is assumed that λ = 0.

Turbulence flows are simulated here using a LES approach, where the fundamental flow equations are submitted to spatial filtering in which the flow field is decomposed into large and small-scale components. Large scales are solved directly utilizing the filtered equations (Eqs. 1 and 2), while scales smaller than the mesh resolution are defined by the subgrid stress tensor $\boldsymbol{\tau}^{\mathrm{SGS}}$, which must be modeled considering a turbulence closure model. Turbulence models are utilized in order to represent the small-scale effects on the large scales. The subgrid stress tensor components $\boldsymbol{\tau}_{ij}^{\mathrm{SGS}}$ are usually approximated according to the Boussinesq assumption, that is:

$$\tau_{ij}^{SGS} = 2\mu_t S_{ij} \tag{5}$$

where S_{ij} are components of the filtered strain rate tensor. When laminar flows are investigated, the subgrid stress tensor components $\boldsymbol{\tau}_{ij}^{\mathrm{SGS}}$ are omitted in Eq. (1).

In the present work, the eddy viscosity μ_t may be obtained considering the Smagorinsky's subgrid-scale model, which may be expressed as follows:

$$\mu_t = \rho C_S \bar{\Delta}|\mathbf{S}| \tag{6}$$

where C_S is the Smagorinsky's constant, which must be specified according to the flow characteristics, with values usually ranging from 0.1 to 0.25, and $\bar{\Delta}$ is the characteristic length of the spatial filter, which may be locally defined as $\bar{\Delta} = \sqrt{\Omega_E}$ for a box filter (see Smagorinsky, 1963 for additional details), where Ω_E is the finite element volume referring to element E.

The eddy viscosity μ_t may be also obtained considering the dynamic model (Germano et al., 1991; Lilly, 1992), where the Smagorinsky's constant is substituted by a dynamic coefficient as follows:

$$\mu_t = \rho C(\mathbf{x}, t)\bar{\Delta}|\mathbf{S}| \tag{7}$$

where $C(\mathbf{x},t)$ is the dynamic coefficient, which is a spatial and time dependent variable. The dynamic coefficient is updated over time based on the instantaneous flow field. The expression due to Lilly (1992) is employed here as follows:

$$C(\mathbf{x}, t) = -\frac{1}{2}\frac{\mathrm{L}_{ij}\mathrm{M}_{ij}}{\mathrm{M}_{ij}\mathrm{M}_{ij}} \tag{8}$$

with:

$$\mathrm{L}_{ij} = \left\langle v_i v_j \right\rangle - \left\langle v_i \right\rangle \left\langle v_j \right\rangle; \qquad \mathrm{M}_{ij} = \left\langle \Delta^2 \right\rangle \left| \left\langle \mathbf{S} \right\rangle \right| \left\langle S_{ij} \right\rangle - \left\langle \Delta^2 |\mathbf{S}| S_{ij} \right\rangle \tag{9}$$

Equation (8) requires a second filtering procedure related to a second test filter $\langle\Delta\rangle$, which must be larger than the first filter $\bar{\Delta}$. In the present work, the test filter is obtained locally considering all the finite elements that are common to a given nodal point. Second filter variables are identified with symbol $\langle\cdot\rangle$ and computed using the following expression:

$$\left\langle k \right\rangle^i = \frac{\sum_{j=1}^{n} \left(\frac{k^j}{d_i^j} \right)}{\sum_{j=1}^{n} \left(\frac{1}{d_i^j} \right)} \tag{10}$$

where k^j is a large-scale generic variable associated with the first filter and defined at a nodal point j, n is the number of nodal points constituting the second filter, d_i^j is the Euclidian distance between the nodal points i and j. The test filter characteristic length is determined by $\langle\Delta\rangle^i = \sqrt[3]{\sum_{j=1}^{ne} \Omega_j}$, where ne is the number of elements constituting the test filter associated with the nodal point i and Ω_j is the finite element volume referring to element j.

In order to solve the flow problem, initial conditions on the flow variables v_i and p must be specified. In addition, appropriate boundary conditions must also be defined on Γ_t^f, which may be expressed as:

$$v_i = w_i \qquad (i = 1,2,3) \qquad \text{on } \Gamma_{\mathrm{t}}^{\mathrm{fsi}} \tag{11}$$

$$v_i = \bar{v}_i \qquad (i = 1,2,3) \qquad \text{on } \Gamma^{\mathrm{v}} \tag{12}$$

$$p = \bar{p} \qquad \text{on } \Gamma^{\mathrm{p}} \tag{13}$$

$$\sigma_{ij} n_j = \left[-p\delta_{ij} + \tau_{ij} \right] n_j = t_i = \bar{t}_i \qquad (i,j = 1,2,3) \qquad \text{on } \Gamma^{\sigma} \tag{14}$$

where Γ_t^{fsi} (boundary representing the fluid-structure interface), Γ^v (boundary with prescribed velocity $\bar{v}_i$), Γ^p (boundary with prescribed pressure $\bar{p}$) and Γ^σ (boundary with prescribed traction $\bar{t}_i$) are complementary subsets of Γ_t^{Tf}, such that $\Gamma_t^{Tf} = \Gamma_t^{fsi} \cup \Gamma^v \cup \Gamma^p \cup \Gamma^\sigma$. In Eq. (14), n_j are components of the unit normal vector **n** evaluated at a point on boundary Γ^σ. Notice that $w_i = 0$ is considered for points outside the ALE domain or when the immersed body is not moving.

3 PID CONTROL

Buildings and bridges are usually designed as passive structures concerning the wind action. However, with advances observed in the field of control theory (see, e.g., Soong, 1990; Ogata, 2010), intelligent structures can be designed, which can adapt themselves in order to reduce aerodynamic loads and suppress aeroelastic instabilities. In the present work, a PID control scheme is proposed to mitigate pressure suctions over low-rise building roofs by using controlled spoilers attached to the roof windward edge.

A feedback control system is adopted here, where the input $u(t)$ (control variable) is related to the angular orientation of the spoiler (actuator) with respect to the horizontal direction, while the output $y(t)$ (process variable) is associated with the lift aerodynamic force resultant evaluated over the roof surface (sensor). A reference value for the process variable y_{sp} (setpoint) is defined initially, from which a control error e can be evaluated instantaneously over time, considering the difference between the reference value and the output ($e = y_{sp} - y$). Consequently, the control variable must be increased when the control error is positive and decreased otherwise.

A PID controller is defined as a superposition of three control components: proportional (P), integral (I) and derivative (D), which may be expressed as follows (Aström and Hägglund, 1995):

$$u(t) = k_p \left(e_p(t) + \frac{1}{T_i} \int_0^t e(\tau) d\tau + T_D \frac{de_D(t)}{dt} \right) \tag{15}$$

where k_p is the proportional gain constant, while T_i and T_D are the integral and derivative times, respectively. The control errors are defined as:

$$e_p = by_{sp} - y \tag{16}$$

$$e_D = cy_{sp} - y \tag{17}$$

$$e = y_{sp} - y \tag{18}$$

where b and c are coefficients associated with load disturbances and noise measurements, with values ranging from 0 to 1. For standard PID controllers, b and c are set to 1.

The proportional (P) component takes into account the instantaneous error and the integral component (I) is associated with the error over time, while the derivative (D) component is related to the error rate of change, where a forecast for future errors is obtained. Simpler controllers can be defined by using appropriate control parameters. A P controller, for instance, is obtained considering $T_i = \infty$ and $T_D = 0$.

Depending on the values adopted for the controller coefficients, the process may present excessive fluctuations in the output or take a very long time to reach the desired output. In addition, numerical instabilities may arise during a CFD simulation due to rapid changes imposed by the PID controller on the actuator. Therefore, the PID controller coefficients must be defined for a given process using tuning procedures. The classical Ziegler-Nichols methods are utilized in the present work, where numerical simulations are carried out to characterize the process based on static and dynamic models.

In order to implement a PID controller into a numerical code, Eq. (15) has to be discretized. The control components are utilized here in the following form:

$$P(t_k) = k_p (by_{sp}(t_k) - y(t_k)) \tag{19}$$

$$I(t_{k+1}) = I(t_k) + \frac{k_p h}{T_i} e(t_k) \tag{20}$$

$$D(t_{k+1}) = \left(1 - \frac{Nh}{T_D} \right) D(t_k) - k_p N (y(t_{k+1}) - y(t_k)) \tag{21}$$

where t_k denotes a time instant in the time-stepping procedure, h is the sampling period and N is a model parameter, with values ranging from 8 to 20 (Aström and Hägglund, 1995).

4 NUMERICAL MODEL

4.1 Characteristic-based Split (CBS) scheme

The Characteristic-based Split (CBS) scheme is formulated considering a coordinate shift along the flow characteristic directions to remove the advective term from the flow fundamental equations, which permits the use of standard Galerkin procedures in finite element spatial discretizations without the emergence of numerical instabilities. Mesh updating is avoided by using Taylor series approximations in the spatial domain and a split operation is utilized following a numerical procedure proposed initially by Chorin (1968) for incompressible flows in a finite difference context. The split operation enables the use of arbitrary interpolation functions for both the pressure and velocity fields and enhances pressure stability. Additional information on the CBS scheme may be found in Zienkiewicz et al. (2013) and Nithiarasu et al. (2016).

The temporally discretized form of the flow equations are presented here as follows:

Step 1: intermediate velocity

$$\tilde{v}_i = v_i^n - \Delta t \left\{ \left(v_j - w_j\right) \left[\frac{\partial v_i}{\partial x_j} - \frac{\Delta t}{2} \frac{\partial}{\partial x_j} \left(v_k \frac{\partial v_i}{\partial x_k} \right) \right] - \left(\frac{\mu + \mu_t}{\rho} \right) \frac{\partial}{\partial x_j} \left(\frac{\partial v_i}{\partial x_j} \right) \right\}^n \quad (i, j, k = 1, 2, 3) \tag{22}$$

Step 2: pressure calculation

$$\frac{1}{\rho} \frac{\partial}{\partial x_j} \left(\frac{\partial p}{\partial x_j} \right)^{n+1} = \frac{1}{\Delta t} \frac{\partial \tilde{v}_i}{\partial x_i} \qquad (i, j = 1, 2, 3) \tag{23}$$

Step 3: velocity correction

$$v_i^{n+1} = \tilde{v}_i - \Delta t \left[\frac{1}{\rho} \frac{\partial p^{n+1}}{\partial x_i} - \left(v_j - w_j\right) \frac{\Delta t}{2} \frac{\partial}{\partial x_j} \left(\frac{1}{\rho} \frac{\partial p^n}{\partial x_i} \right) \right] \qquad (i, j = 1, 2, 3) \tag{24}$$

A global time increment Δt is defined considering instantaneous flow conditions observed at element level, which leads to the following expression:

$$\Delta t = \min \left(\Delta t_{conv}, \Delta t_{dif} \right) \tag{25}$$

with:

$$\Delta t_{conv} = \frac{l}{\|\mathbf{v}\|}; \qquad \Delta t_{dif} = \frac{l^2}{2Re} \tag{26}$$

where l is the finite element characteristic length, $\mathbf{v}$ is the vector of nodal velocities at element level and Re is the Reynolds number. A safety coefficient is applied to the global time increment obtained from Eq. (25), which usually ranges from 0.5 to 2 according to mesh characteristics and flow complexity.

4.2 Finite element model

The standard Galerkin procedure is adopted here for spatial discretization of the flow equations after a temporal discretization operation is accomplished using the CBS scheme, where linear tetrahedral elements are utilized for both the velocity and pressure fields. Viscous and stabilizing terms are integrated by parts in steps 1 and 3, while the pressure Laplacian is integrated by parts in step 2, leading to boundary integral terms. A system of linear algebraic equations is then obtained for the discretized flow equations, which are expressed in matrix form as:

Step 1:

$$\tilde{\mathbf{v}}_i = \mathbf{v}_i^n - \mathbf{M}_d^{-1} \Delta t \left[\left(\mathbf{A} + \mathbf{D} \right) \mathbf{v}_i - \frac{\Delta t}{2} \mathbf{S}_v \mathbf{v}_i - \mathbf{f}_i \right]^n \qquad (i = 1, 2, 3) \tag{27}$$

Step 2:

$$\mathbf{H}\mathbf{p}^{n+1} = \frac{\rho}{\Delta t} \mathbf{G}_i^T \tilde{\mathbf{v}}_i \qquad (i = 1, 2, 3) \tag{28}$$

Step 3:

$$\mathbf{v}_i^{n+1} = \tilde{\mathbf{v}}_i - \mathbf{M}_d^{-1} \frac{\Delta t}{\rho} \left[\mathbf{G}_i \mathbf{p}^{n+1} + \frac{\Delta t}{2} \left(\mathbf{S}_p \right)_i \mathbf{p}^n \right] \qquad (i = 1, 2, 3) \tag{29}$$

where $\mathbf{v}_i$ and $\mathbf{w}_i$ are the flow and mesh velocity vectors evaluated at nodal level, $\mathbf{p}$ is the pressure nodal vector and $\mathbf{M_d}$ is the discrete mass matrix, which is obtained from the consistent mass matrix $\mathbf{M}$ using the row sum technique. The finite element matrices are defined here as follows:

$$\mathbf{M}=\bigcup_{E=1}^{NEL}\left(\int_{\Omega_E}\mathbf{N}^T\mathbf{N}\,d\Omega\right);\quad \mathbf{S}_v=\bigcup_{E=1}^{NEL}\left(\int_{\Omega_E}\left[\mathbf{N}\left(\mathbf{v}_i^n-\mathbf{w}_i^n\right)\right]\left[\mathbf{N}\left(\mathbf{v}_j^n-\mathbf{w}_j^n\right)\right]\frac{\partial\mathbf{N}^T}{\partial x_i}\frac{\partial\mathbf{N}}{\partial x_j}d\Omega\right);$$

$$\mathbf{D}=\bigcup_{E=1}^{NEL}\left(\frac{\mu+\mu_t}{\rho}\int_{\Omega_E}\frac{\partial\mathbf{N}^T}{\partial x_j}\frac{\partial\mathbf{N}}{\partial x_j}d\Omega\right);\quad \mathbf{f}_i=\bigcup_{E=1}^{NEL}\left(\frac{1}{\rho}\int_{\Gamma_E}\mathbf{N}^T t_i\,d\Gamma\right);\quad \mathbf{G}_i=\bigcup_{E=1}^{NEL}\left(\int_{\Omega_E}\mathbf{N}^T\frac{\partial\mathbf{N}}{\partial x_i}d\Omega\right);$$

$$\mathbf{A}=\bigcup_{E=1}^{NEL}\left(\int_{\Omega_E}\left[\mathbf{N}\left(\mathbf{v}_j^n-\mathbf{w}_j^n\right)\right]\mathbf{N}^T\frac{\partial\mathbf{N}}{\partial x_j}d\Omega\right);\quad \mathbf{H}=\bigcup_{E=1}^{NEL}\left(\int_{\Omega_E}\frac{\partial\mathbf{N}^T}{\partial x_i}\frac{\partial\mathbf{N}}{\partial x_i}d\Omega\right);\tag{30}$$

$$\left(\mathbf{S}_p\right)_i=\bigcup_{E=1}^{NEL}\left(\int_{\Omega_E}\left[\mathbf{N}\left(\mathbf{v}_j^n-\mathbf{w}_j^n\right)\right]\frac{\partial\mathbf{N}^T}{\partial x_j}\frac{\partial\mathbf{N}}{\partial x_i}d\Omega\right)$$

where **N** is a row matrix containing the interpolation functions associated with the linear tetrahedral element.

The aerodynamic forces are locally evaluated considering any finite element sharing an element face with a fluid-structure interface, which may be expressed as:

$$\left(\mathbf{F}_i\right)_E=\int_{\Gamma_E}\mathbf{N}^T\left[\left(\mathbf{N}\bar{\mathbf{p}}\right)n_i-\left(\mu+\mu_t\right)\left(\frac{\partial\mathbf{N}}{\partial x_j}\bar{\mathbf{v}}_i\right)n_j\right]d\Gamma\qquad (i,j\ =\ 1,2,3)\tag{31}$$

where $\bar{\mathbf{v}}_\mathbf{i}$ and $\bar{\mathbf{p}}$ are the flow velocity and pressure local vectors, while n_j are components of the unit normal vector **n** evaluated at a point on the interface. By using a typical finite element assembly procedure, aerodynamic force vectors $\mathbf{F}_I$ are then evaluated at nodal level. The aerodynamic force and moment resultants at a specific point P are finally obtained with:

$$\mathbf{F}_R=\sum_{I=1}^{NNI}\mathbf{F}_I;\qquad \mathbf{M}_R^P=\sum_{I=1}^{NNI}\left(\mathbf{r}_{PI}\times\mathbf{F}_I\right)\tag{32}$$

where *NNI* is the number of nodal points on the fluid-structure interface and $\mathbf{r}_{PI}$ is a position vector defined between points P and I.

4.3 Spoiler and mesh motion scheme

The roof spoilers are considered here using the rigid body assumption, where its motion is governed by the control algorithm presented previously. In the present model, spoilers can only rotate around the rotation axis at its trailing edge, as shown in Figure 1. In order to accommodate the spoiler motion within the flow spatial field, an ALE kinematic formulation and a mesh motion scheme are adopted.

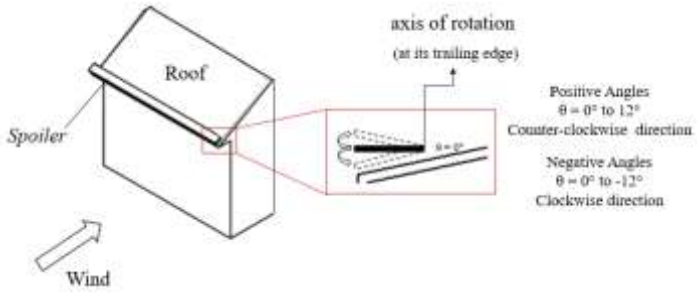

Figure 1: Spoiler Movement

The flow problem on moving grids is adequately solved if the geometric conservation law (GCL) is satisfied (see Thomas and Lombard (1979) for detailed information). According to Lesoinne and Farhat (1996), the GCL is satisfied in ALE finite element formulations if the mesh velocity vector **w** is calculated as:

$$\mathbf{w}=\mathbf{v}=\frac{\mathbf{x}_{n+1}-\mathbf{x}_n}{\Delta t}\qquad \text{on } \Gamma_{\mathrm{t}}^{\mathrm{fsi}}\tag{33}$$

where $\mathbf{x}_n$ and $\mathbf{x}_{n+1}$ are nodal coordinate vectors referring to nodes belonging to moving fluid-structure interfaces, which are evaluated at time instants t_n and t_{n+1} within the time interval $\Delta t = t_{n+1} - t_n$.

The mesh motion is arbitrarily defined according to the spoiler motion. In this work, a mesh motion scheme utilized by Braun and Awruch (2008) and [b]Braun and Awruch (2009) is employed, where the mesh velocity components are obtained as follows:

$$w_k^i = \frac{\sum_{j=1}^{NS} a_{ij} w_k^j}{\sum_{j=1}^{NS} a_{ij}} \qquad (k = 1,2,3) \tag{34}$$

where *NS* is the number of mesh points located on the boundaries of the ALE domain and a_{ij} are influence coefficients defined with mesh points *i* and *j*, considering that *i* are inner mesh points and *j* are mesh points belonging to the boundaries of the ALE domain, where $w_i = 0$. The influence coefficients are obtained with:

$$a_{ij} = \left(d_{ij} \right)^{-n} \tag{35}$$

where d_{ij} is the Euclidian distance between the mesh points *i* and *j* and exponent *n* is a user-defined parameter, which is chosen according to the amplitude of the immersed body displacements. In this work, all applications were analyzed using $n = 4$.

The flow velocity vector referring to nodes belonging to the spoiler surface is calculated here considering that the spoiler motion is restricted to rigid body rotations around the rotation axis, and the no-slip condition is adopted, which leads to:

$$\mathbf{v}_{int}(t_{n+1}) = \boldsymbol{\omega}^s(t_{n+1}) \times \mathbf{r}_{o,int}(t_{n+1}) \tag{36}$$

where $\mathbf{r}_{o,int}$ is the position vector defined between a point on the rotation axis (*o*) and a point on the spoiler surface (*int*). The spoiler angular velocity vector $\boldsymbol{\omega}^s$ is obtained taking into account the angular position given by the control algorithm (Eq. 15) within a time interval. Considering the rotation axis is aligned with the global coordinate axis Z, the spoiler angular speed is evaluated here as follows:

$$\omega_z(t_{n+1}) = \frac{u(t_{n+1}) - u(t_n)}{\Delta t} \tag{37}$$

where *u* is the control variable obtained from Eqs. (15) to (21), which defines the spoiler angular position instantaneously.

The position of fluid nodes in the ALE domain is then updated considering the following expression:

$$\mathbf{x}_{n+1} = \mathbf{x}_n + \mathbf{w}\Delta t \tag{38}$$

where **w** is the mesh velocity vector, which is evaluated considering Eqs. (33) and (34).

4.4 Numerical algorithm

The pressure mitigation methodology proposed here for reducing the aerodynamic loading on low-rise building roofs may be briefly described using the following numerical algorithm:

1) Solve the flow problem using Eqs. (27) to (29) and boundary conditions specified by Eqs. (11) to (14);
2) Obtain the aerodynamic forces induced by the wind flow on roof surfaces with sensors (see Eqs. 31 and 32);
3) Determine the spoiler angular orientation from PID control, Eqs. (15) to (21);
4) Calculate the spoiler instantaneous angular speed using Eq. (37);
5) Calculate the instantaneous flow velocity vector for nodes on the spoiler surface using Eq. (36);
6) Obtain the instantaneous mesh velocity vector over the ALE domain considering the mesh motion scheme defined by Eq. (34) and boundary condition expressed by Eq. (11);
7) Update the position of fluid nodes in the ALE domain using Eq. (38);

Return to step 1 and proceed to the next time step until the time integration process is concluded.

For the numerical investigation performed here, sensors were considered at all mesh points on the roof surface. In a practical project, a detailed analysis would be required to determine the location of the sensors optimally. The most suitable locations for their installation correspond to regions near the roof edges, where the highest suction pressures occur, specifically along the edges where flow separation takes place.

5 NUMERICAL EXAMPLES

The examples presented in this section were first analyzed by Loredo-Souza (1992) (see also Loredo-Souza, 1995) using wind tunnel simulation. In the experimental tests, an isolated building subject to different wind flow incidences was investigated, considering impermeable models and some combinations of wall openings. In addition, turbulent boundary layer and smooth uniform flows were also considered. Figure 2 shows details on the computational domain utilized here, where boundary conditions, geometry of the building model and opening locations are indicated. Physical and numerical parameters used in the present simulations are presented in Table 1, which correspond to a flow with smooth and uniform conditions.

Table 1 Physical and numerical parameters.

Parameter	Values
Specific mass (ρ)	1.2249 Kg/m³
Dynamic viscosity (μ)	4.679×10^{-5} Ns/m²
Reference speed (V_∞)	30.00 m/s
Reference dimension – building height (H)	0.17825 m
Smagorisky's constant (Cs)	0.1
Reynolds number (Re)	1.4×10^5

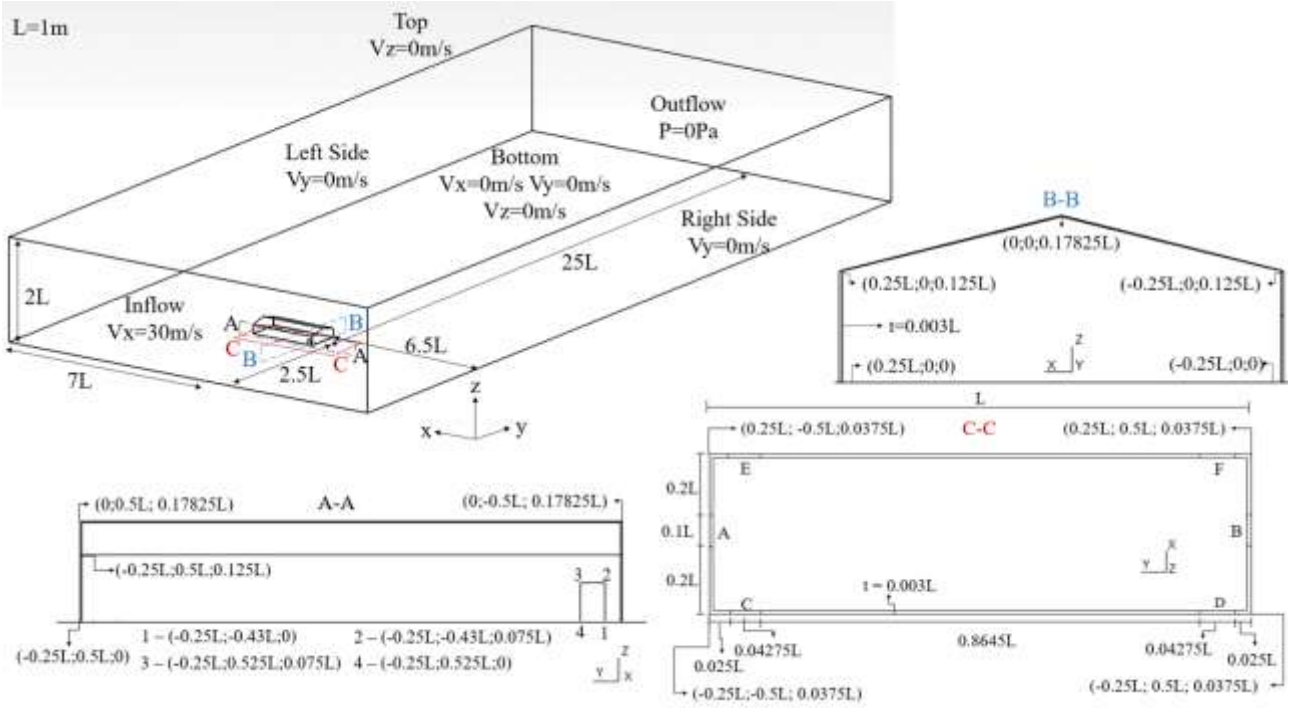

Figure 2: Computational domain, boundary conditions and building geometry

Low-rise buildings subject to wind action develop strong vortices on the roof areas, specifically at the transition between wall and roof, which generate high suction peaks in these regions. When openings are located on the windward wall, large positive pressures are transmitted to the internal environment of the building and a combination between external and internal pressures may result in intense lift loads on the roof structure. In this sense, this work proposes a numerical investigation on the distribution of external and internal pressures in a low-rise building model, where automatically controlled spoilers are utilized to reduce the lift force resultant acting on the roof. Numerical predictions obtained with the numerical model proposed here are compared initially with experimental results obtained by Loredo-Souza (1992) using wind tunnel techniques in order to validate the finite element formulation, where a building model with no spoilers is utilized.

Two-dimensional simulations are performed first considering the building section cuts B-B and C-C, as illustrated in Fig. 2. These preliminary analyses are carried out using a two-dimensional approach and a LES-type model with adjustment of the Smagorinky's constant. Although the LES methodology is an inherently three-dimensional approach, a two-dimensional analysis can also be adopted approximately in the case of flows with homogeneous longitudinal

fluctuations (Bruno and Khris, 2003). In addition, it is important to notice that this initial investigation is mainly utilized to calibrate the PID control model.

The C-C section cut simulations intend to evaluate the circulation around and inside the building. Simulations with the B-B section cut, in contrast, refer to the evaluation of critical loads on the building roof, as described above, where cases with and without opening are simulated considering the insertion of a fixed spoiler, as a manner to obtain the necessary parameters for the elaboration of the PID control theory and model calibration.

Three-dimensional analyses complete the present investigation, where the worst building configuration in terms of pressure resultant on the roof and a building configuration with impermeable walls are simulated. Comparisons are performed considering the experimental results obtained by Loredo-Souza (1992) and the two-dimensional predictions obtained during the preliminary analyses. A building model with an opening on the front wall and continuous spoilers along the windward and downward roof edges is also analyzed using the proposed PID control algorithm and parameters obtained from the two-dimensional calibration.

5.1 Preliminary analyses – two-dimensional simulations

5.1.1 Analysis of pressure distribution and circulation

Six building configurations using the C-C section cut are simulated considering two models with impermeable walls and subject to parallel as well as perpendicular wind flows and four models with wall openings, as indicated in Table 2. These preliminary analyses are important for validating the algorithm and understanding the pressure resultants on the roof structure, considering the external and internal environments according to the different building configurations proposed here. Mesh characterization is also presented in Table 2, taking into account the number of finite elements and nodes used in the spatial discretization procedure. A mesh quality analysis is performed first considering the test cases *galp01* and *galp02* and three discretization configurations characterized by the following dimensionless wall distances y^+: 4.990, 4.109 and 0.990. The smallest element length is kept constant for elements next to building surfaces and regions around the body and wake, having values from $1.0\text{x}10^{-4}L$ to $3.0\text{x}10^{-4}L$, where L = 1 m is the building length.

Table 2 Two-dimensional test cases investigated and the corresponding mesh characteristics.

Test case	Wind direction	Openings	Number of nodes	Number of elements
galp01 *y*+ = 4.109	90°	-	235,534	702,741
galp01 *y*+ = 4.99	90°	-	115,186	639,852
galp01 *y*+ = 0.99	90°	-	1,002,964	2,182,673
galp02 *y*+ = 4.109	0°	-	354,254	1,058,664
galp02 *y*+ = 4.99	0°	-	221,440	813,852
galp02 *y*+ = 0.99	0°	-	998,474	2,558,542
galp03	0°	D	394,872	1,177,347
galp04	90°	A	394,872	1,177,347
galp05	90°	A, D and F	394,872	1,177,526
galp06	0°	A, D and F	498,942	1,490,088

The location of measurement points for evaluation of external pressure is shown in Fig. 3 and 4, which is based on positions utilized by Loredo-Souza (1992). External pressure distributions obtained for the first two test cases analyzed here are shown in Figure 3 and 4, which are compared with experimental results presented by Loredo-Souza (1992) and pressure distributions obtained according to the Brazilian standard NBR6123 (ABNT, 1988).

The present results show good agreement in general with the experimental predictions when the test case *galp01* is considered, indicating that the finite element mesh associated with the dimensionless wall distance y^+ = 4.109 and the value utilized here for the Smagorinsky's constant are adequate in this case. Although the pressure values obtained numerically for the test case *galp02* are higher than those obtained from the experimental tests, the pressure distributions over the building walls are similar for both approaches. One can also observe that pressure results suggested by the Brazilian standard NBR6123 are overpredicted with respect to experimental and numerical predictions for most of the measurement points evaluated here, where windward walls are submitted to positive pressure, while suction

pressure is observed on the leeward and lateral walls, as expected. Table 3 presents results related to force coefficients obtained over the building walls, where time-mean and r.m.s. values are calculated using the following equations:

$$C_x = \frac{\sum_{i=1}^{NNI}(F_x)^i}{\frac{1}{2}\rho V_\infty^2 WH}; \qquad C_y = \frac{\sum_{i=1}^{NNI}(F_y)^i}{\frac{1}{2}\rho V_\infty^2 HL}; \qquad C_z = \frac{\sum_{i=1}^{NNI}(F_z)^i}{\frac{1}{2}\rho V_\infty^2 WL} \tag{39}$$

where *W* and *L* are the building width and length in the wind incidence facade and $(F_x)^i$, $(F_y)^i$ and $(F_z)^i$ are flow-induced forces evaluated at a nodal point *i* on the immersed body surface, which are obtained using Eq. (31). The present results are compared with the drag force coefficient predicted by the Brazilian standard NBR6123, where a good agreement is also observed.

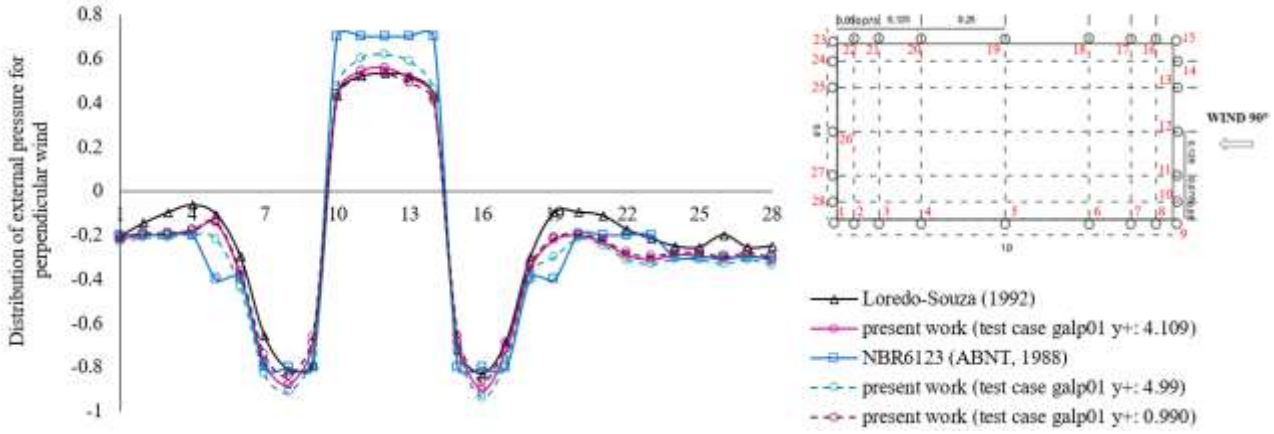

Figure 3: Distribution of external pressure for perpendicular wind incidence.

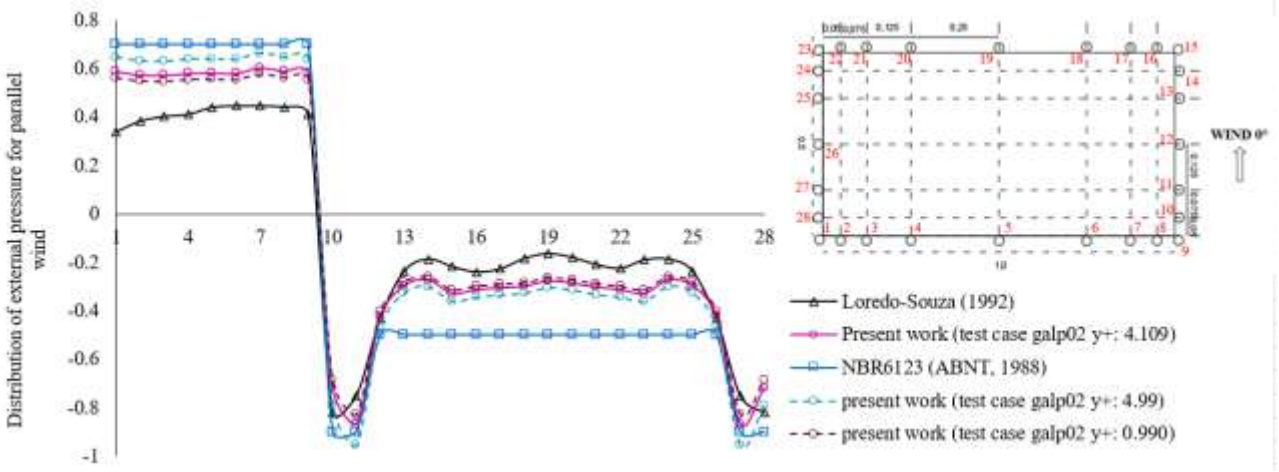

Figure 4: Distribution of external pressure for parallel wind incidence.

Table 3 Two-dimensional test cases investigated and the corresponding mesh characteristics.

Test cases/reference	Wind direction	Openings	Cx_m	Cx_{rms}	Cy_m	Cy_{rms}
galp01 (y+ = 4.109)	90°	-	1.135	0.151	-0.049	0.262
galp01 (y+ = 4.99)	90°	-	1.275	0.322	-0.031	0.299
galp01 (y+ = 0.99)	90°	-	1.131	0.078	-0.045	0.219
NBR 6123	90°	-	1.000	-	-	-

A time-averaged pressure distribution obtained here for the flow field around the building model corresponding to the test case *galp03* is shown in Figure 5, where one can see that the opening configuration utilized in this case causes a high positive pressure on the front wall and inside the building. In this case, the maximum and minimum values found delimit the analyzed range. This configuration is used in the subsequent analyses in order to elaborate the PID control

theory for the controlled spoiler, considering that the worst loading scenario for the roof structure is observed when internal positive pressure and external suction are combined.

Three additional simulations are carried out considering different opening configurations for the building model analyzed here, which correspond to the test cases *galp04*, *galp05* and *galp06* indicated in Table 2 (see Fig. 2 for opening locations). Internal pressure coefficients are obtained numerically according to the position of measurement points presented in Fig. 6. From the internal pressure coefficients evaluated locally with the corresponding influence areas, a single representative value for the internal environment is calculated using a simple average procedure. A comparison is carried out taking into account the wind tunnel results obtained by Loredo-Souza (1992) and predictions based on the Brazilian standard NBR6123 (ABNT, 1988). The results presented in Table 4 demonstrate good agreement between numerical and experimental predictions, indicating that a two-dimensional LES-type approach with the C-C section cut is able to reproduce satisfactorily inner flow conditions for the building configurations and flow characteristics analyzed in this work. A reasonable agreement is observed when the present results are compared with the standard predictions provided by NBR6123 (ABNT, 1988), except for the test case *galp04*, where numerical and experimental results present significantly lower values. Snapshots of the flow conditions around and inside the building models analyzed here are shown in Fig. 6, where instantaneous pressure fields for the test cases *galp04*, *galp05* and *galp06* are presented. Notice that the test case *galp04* leads to high positive pressures throughout the internal environment, producing overload conditions on the roof structure. On the other hand, favorable conditions for the roof structure are obtained using the building configurations referring to the test case *galp06*, where moderate positive pressures and suctions are observed internally. The maximum and minimum values found in any of the cases determine the pressure range analyzed.

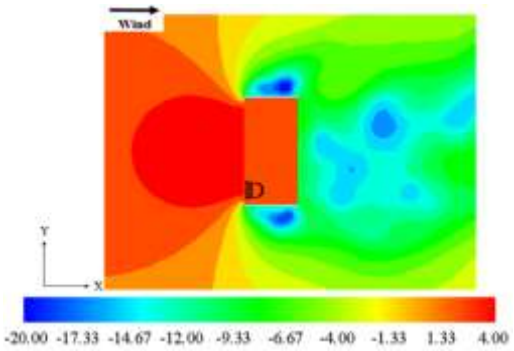

Figure 5: Time-averaged pressure field for the test case galp03.

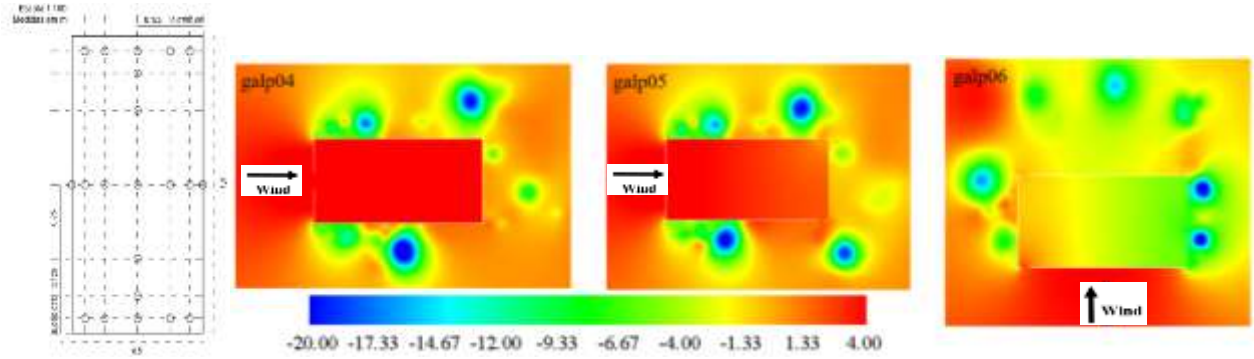

Figure 6: Instantaneous pressure fields around and inside the building models galp04, galp05 and galp06.

Table 4 Permeable building: comparison of time-averaged internal pressure coefficients.

Test case	Wind direction	Openings	100Ci mean (Loredo-Souza,1992)	100Ci mean (NBR6123)	100 Ci mean (present work)	100Ci extrema (Loredo-Souza, 1992)	100Ci extrema (present work)
galp04	90°	A	52	80	51	52; 52	50; 52
galp05	90°	A, D and F	23	30	29	20; 32	23; 35
galp06	0°	A, D and F	-36	-20	-33	-42; -25	-38; -25

5.1.2 Development of the PID control theory

The building configurations corresponding to cases *galp02* and *galp03* (see Table 2) are utilized here to develop the PID control formulation for spoiler operation, where a two-dimensional LES-type approach is employed using the B-B section cut. Spoilers are employed along the windward and downward roof edges to reduce the aerodynamic loading on the building roof, considering that only the windward spoiler is activated by the control system. By using the present simulations, one can obtain model parameters to calibrate the PID control algorithm. The computational domain and boundary conditions adopted here are the same as those shown in Figure 2, taking into account the B-B section cut, and details about the building and spoiler geometries are presented in Fig. 7. A mesh quality analysis is performed first considering three discretization configurations characterized by the following dimensionless wall distances y^+: 4.875, 2.739 and 0.961. The finite element mesh obtained with y^+ = 2.739 is then used in the numerical simulations, which presents the smallest element size around $2x10^{-4}L$ for elements next to the building and spoiler surfaces. The spoiler is hinged at the right end (edge) and rotation is allowed around the *y*-axis of the adopted coordinate system, varying between the counterclockwise and clockwise directions from the horizontal orientation (spoiler at 0°), with a maximum amplitude of ±12°. No-slip conditions are imposed on the building and spoiler surfaces.

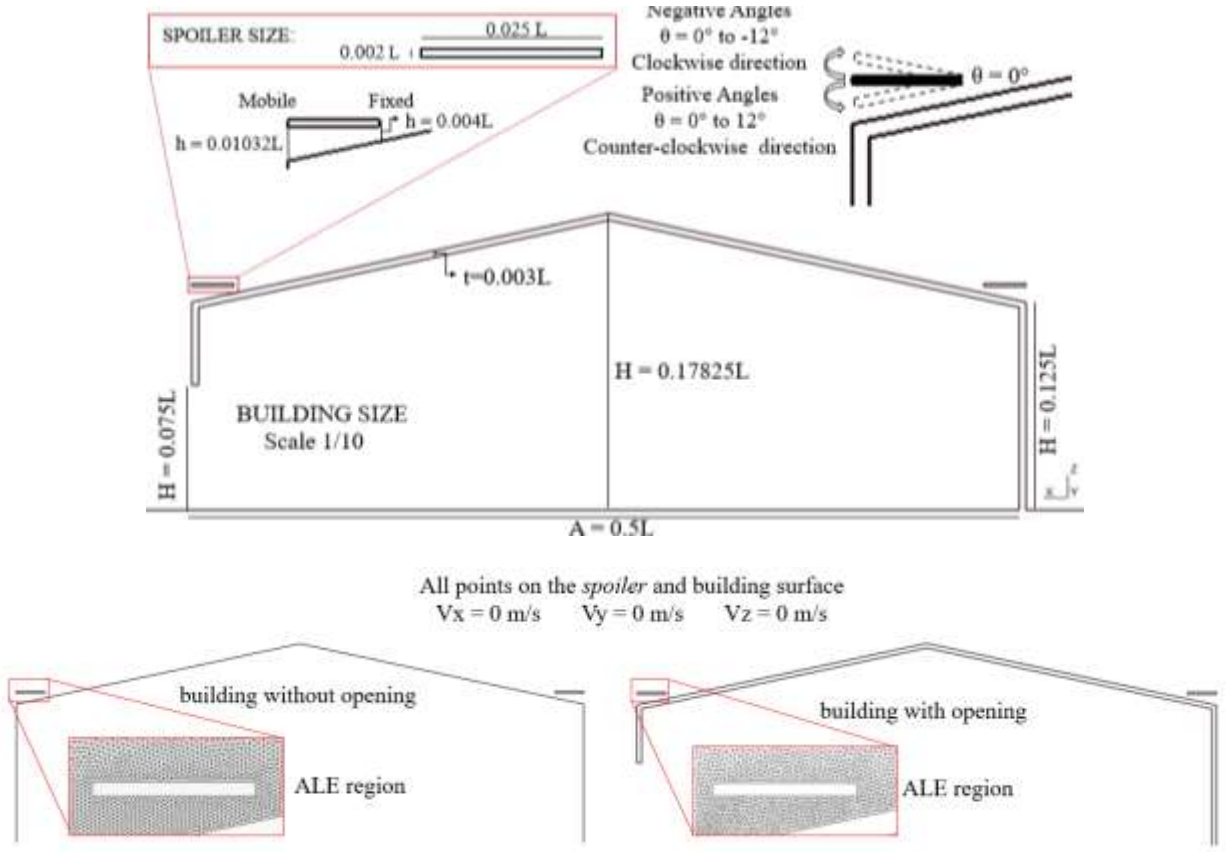

Figure 7: Description of the building and spoiler geometric characteristics and details of ALE region – B-B section cut.

Results obtained here during the mesh quality analysis are summarized in Table 5, where one can see that predictions produced using a mesh configuration with *y*+ = 2.739 is able to provide satisfactory results. The acronyms *sa* and *ca* utilized in Tables 5 and 6 denote building configurations without and with opening, respectively, while *sa* and *sh* indicate the spoiler orientation in the counterclockwise and clockwise directions. The last two digits inform the spoiler orientation angle given in terms of degrees.

Figure 8 presents results related to a brief study carried out here in order to define a positioning height of the spoiler that minimizes the wind load on the roof structure. The positioning height suggested by Li et al. (2018) (h = 0.004L) is utilized and two additional heights are also evaluated: h = 0.002L and h = 0.006L. As can be seen in Fig. 8, the average pressure fields above the building indicate the positioning height of h = 0.004L represents the most satisfactory configuration for mitigating pressure loads on the roof, significantly reducing the wind forces acting in these regions.

Therefore, that positioning height is adopted in the following simulations. The maximum and minimum values found in any of the cases determine the pressure range analyzed.

Table 5 Time-mean and r.m.s. force coefficients over the building walls – C-C section cut.

Test case	Number of elements	C_{zm} Windward	C_{xm} Windward
sash00 (y+ = 4.875)	$5.1x10^5$	0.710	-0.261
sash00 (y+ = 2.739)	$1.5x10^6$	0.645	-0.232
sash00 (y+ = 0.961)	$2.9 x10^6$	0.627	-0.226
cash00 (y+ = 4.875)	$7.8x10^5$	0.894	-0.308
cash00 (y+ = 2.739)	$1.7x10^6$	0.800	-0.268
cash00 (y+ = 0.961)	$3.2 x10^6$	0.779	-0.263

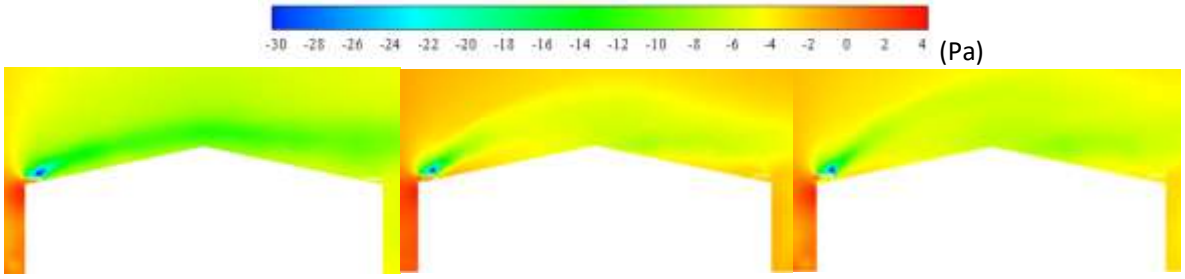

(a) (b) (c)

Figure 8: Pressure fields over the building for different positioning heights of the spoiler: (a) h = 0.002L; (b) h = 0.004L; (c) h = 0.006L.

Simulations of a total of 28 test cases are performed and the corresponding results in terms of aerodynamic coefficients and Strouhal number are presented in Table 6. This information is fundamental for elaborating the PID control theory and represents an initial study, entitled static analysis, where some model parameters are obtained. Additional parameters are obtained later using complementary evaluations based on dynamic analysis. Finally, two-dimensional simulations are carried out to verify the control formulation with parameters obtained from the static and dynamic analyses. All the investigation steps employed here for the development of the PID control model are summarized in Fig. 9.

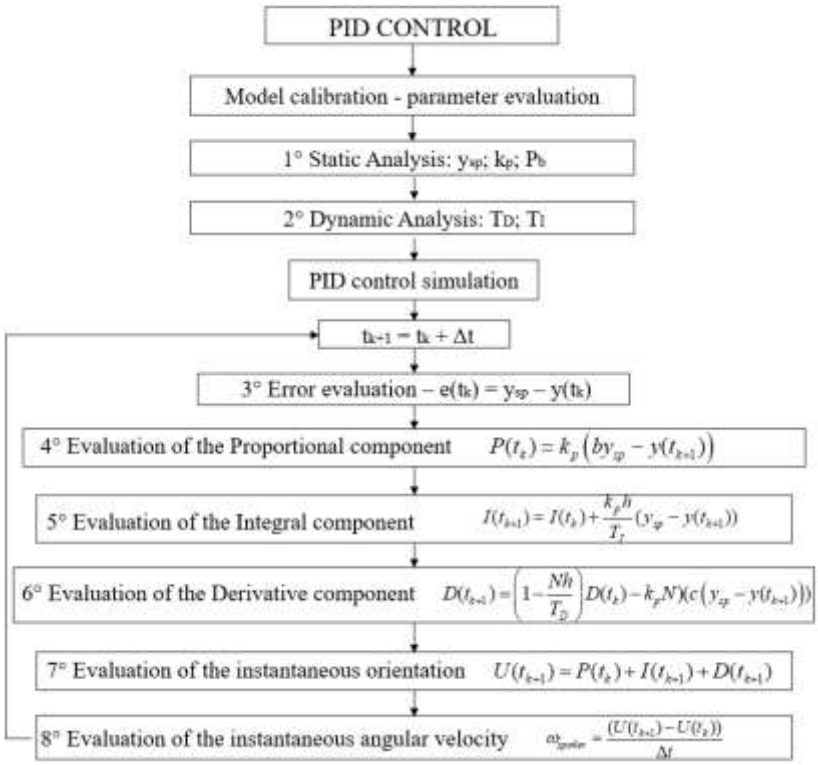

Figure 9: Development of the PID control model.

Time-averaged force coefficients are calculated according to the force components in the *x* and *z* directions of the coordinate system (see Eq. 39), which are evaluated considering the windward and downward roof regions independently, were *H* is the building height in the point measure, *L* = 0.5 m is the building length on the wind incidence façade, and *W* = 1m in this cases. In addition, the Strouhal number (S_t) referring to the windward spoiler is presented. Parameters and time-averaged fields are calculated from the time instant *t* = 40 s, when the flow is fully developed and the vortex street is well defined in the wake region. The Strouhal number for the windward spoiler is calculated here utilizing the following expression:

$$S_t = \frac{f_s D}{V_\infty} \tag{40}$$

where f_s is vortex shedding frequency evaluated at the spoiler, V_∞ is the flow reference speed (see Table 1) and *D* is the body characteristic dimension, which is associated here with the height where the spoiler free end is positioned (see Fig. 6).

Table 6 Time-averaged force coefficients: impermeable and permeable conditions.

Spoiler angle	Test case	C_{zm} Windward	C_{xm} Windward	C_{zm} Leeward	*St* Spoiler	Teste Case	C_{zm} Windward	C_{xm} Windward	C_{zm} Leeward	*St* Spoiler
-	sa0000	1.454	-0.511	0.925	-	ca0000	1.220	-0.418	1.022	-
-12	sash12	0.510	-0.165	0.764	0.765	cash12	0.701	-0.235	0.925	0.630
-10	sash10	0.457	-0.149	0.714	0.615	cash10	0.688	-0.231	0.933	0.492
-8	sash08	0.413	-0.166	0.653	0.555	cash08	0.689	-0.232	0.923	0.422
-6	sash06	0.494	-0.161	0.718	0.497	cash06	0.684	-0.230	0.911	0.419
-4	sash04	0.539	-0.176	0.764	0.395	cash04	0.684	-0.231	0.938	0.351
-2	sash02	0.511	-0.168	0.715	0.261	cash02	0.770	-0.258	0.920	0.218
0	sash00	0.645	-0.232	0.689	0.119	cash00	0.800	-0.268	0.915	0.151
2	sasa02	0.645	-0.212	0.796	0.130	casa02	0.876	-0.298	0.982	0.118
4	sasa04	0.639	-0.249	0.696	0.107	casa04	1.020	-0.347	0.898	0.053
6	sasa06	0.746	-0.286	0.698	0.074	casa06	0.980	-0.330	0.898	0.064
8	sasa08	0.851	-0.269	0.685	0.042	casa08	0.945	-0.320	0.908	0.074
10	sasa10	0.808	-0.269	0.683	0.052	casa10	1.028	-0.348	0.904	0.042
12	sasa12	0.817	-0.273	0.681	0.052	casa12	1.007	-0.339	0.903	0.052

Although the wind action on the leeward roof is relevant to the structural design, small modifications are observed in terms of pressure suction on that roof area as the windward spoiler is rotated, as indicated by C_{zm} values obtained in the leeward roof. Therefore, the windward spoiler is controlled here considering only the flow-induced forces evaluated in the windward roof region, while the leeward spoiler is maintained parallel to the horizontal direction. Notice that leeward spoilers with horizontal orientation do not alter the pressure distribution on the roof significantly (Li et al., 2018). However, spoilers must be placed on both sides of the roof in order to take into account different directions of wind incidence. Nevertheless, no spoiler rotation is needed when the wind is blowing against the opposite building facade.

According to the results presented in Table 6, one can see that the drag and uplift forces on the windward roof are significantly reduced for spoiler orientations within the clockwise rotation interval (negative angles). In this case, high suction peaks are minimized due to deviation of vortices from the roof surface, which were previously found very close to the roof. It is noteworthy that the presence of a spoiler with any orientation is sufficient to change considerably the pressure field and flow-induced forces on the roof. Even for spoiler angles where the load mitigation is not significant, the force coefficients are still reduced about 16% with respect to the case where no spoiler is utilized. For spoiler angles where the load mitigation is more efficient, the average reduction may reach levels of 45%.

Results referring to force coefficients on the windward spoiler are shown in Fig. 10 as functions of the spoiler rotation angle, where one can observe that the lift force intensity on the spoiler directly depends on its orientation. The wind loading on the spoiler is significantly increased for spoiler orientations with angles in the negative range (clockwise direction), especially when a building configuration with opening is considered. This interval of spoiler orientations corresponds to the interval where the load mitigation observed over the windward roof region is more significant. On the other hand, the flow-induced loads on the spoiler are smaller for spoiler orientations with angles in the positive range

(counterclockwise direction), for which the mitigation efficiency is not optimized. Load evaluations are important for aerodynamic appendix design, where material deformations may influence the load mitigation efficiency. Predictions obtained in the present investigation correspond to spoiler materials with high stiffness and robust fixation mechanisms.

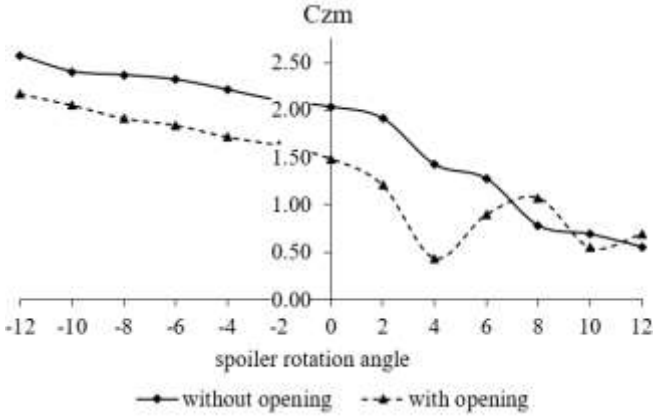

Figure 10: Aerodynamic loading on the windward spoiler: time-averaged force coefficients in the z direction.

The highest mitigation levels are observed when the spoiler orientation corresponds to spoiler angular values in the negative range (clockwise direction). In addition, the higher reduction percentages are obtained when a building configuration without opening is considered, where a reduction of 85% in the spatial average of the pressure coefficient C_{Pm} is observed over the windward roof region. For positive angles (counterclockwise direction), peaks of pressure suction still exist, but less intense when compared with the corresponding results obtained using a building configuration with no spoiler. Although the load mitigation evaluated in the present investigation shows lower efficiency when spoiler angles in the positive range are adopted, some reduction in the loading level is always observed for the range of orientation angles analyzed here. Notice that spoiler orientations with clockwise direction are able to suppress the development of pressure suction peaks previously found on the roof leading-edge. In addition, a deviation of the vortex street can be identified, such that the vortices shed from the windward region are not interacting directly with the roof surface anymore, indicating that the presence of flow disturbers plays an important role in mitigating pressure loads on the roof structure.

Some instantaneous pressure fields are shown in Figs. 11 and 12 considering all the spoilers orientations analyzed in the present investigation, where building configurations with and without opening are utilized. The maximum and minimum values found in any of the cases determine the pressure range analyzed.

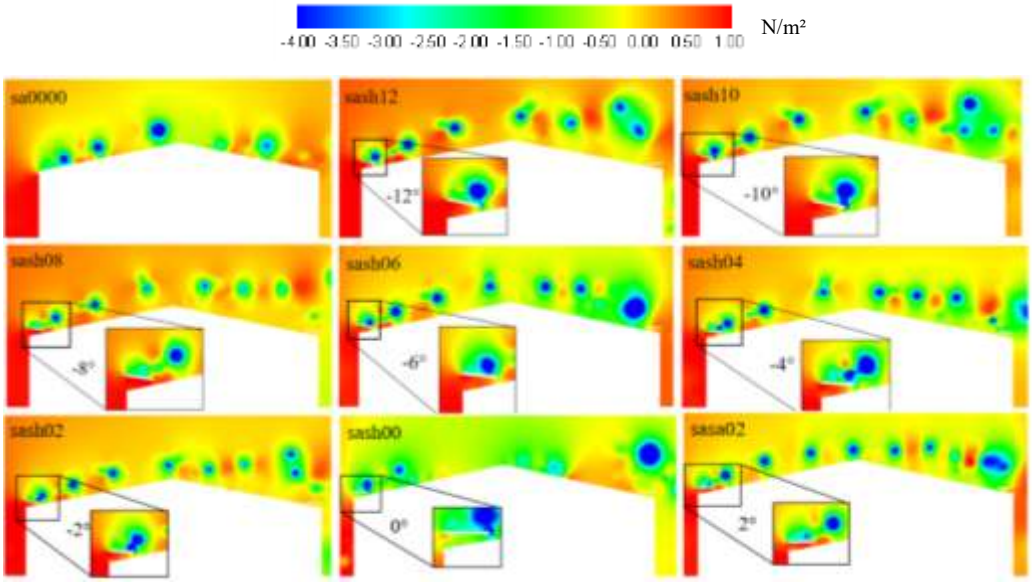

Figure 11: Instantaneous pressure fields for building configurations without opening.

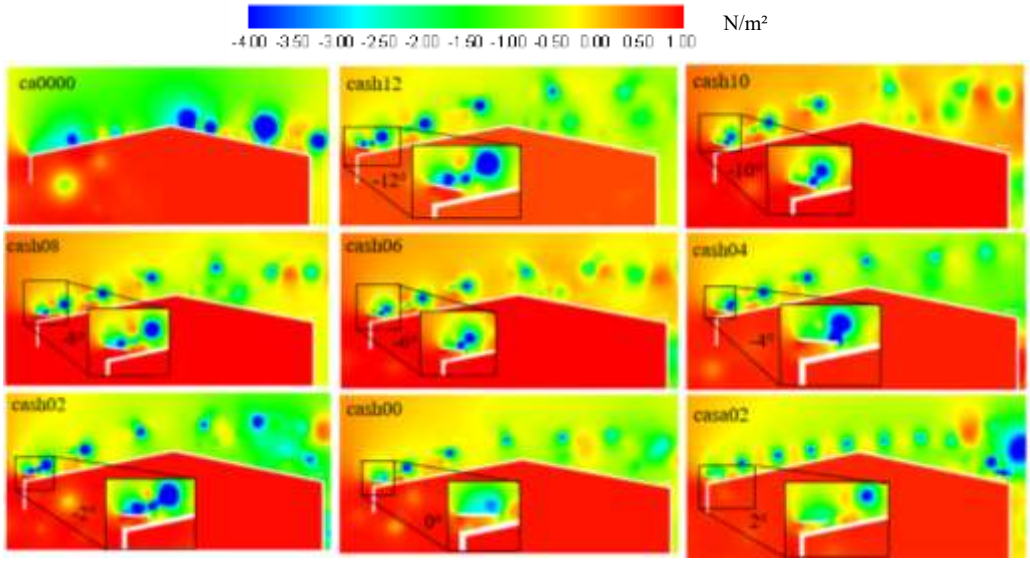

Figure 12: Instantaneous pressure fields for building configurations with opening.

Snapshots of the flow field around the building location demonstrate the importance of the vortex shedding phenomenon on the development of aerodynamic loading induced by the wind on the roof surface. One can see clearly that large vortices are shed from the leading-edge of the roof when a building configuration without opening and without spoiler (*sa*0000) is analyzed. These large vortices generate high pressure suctions on the roof surface, which are usually transferred to the roof structure through important uplift forces.

Spoiler orientations with negative angles (clockwise direction) generate significant reductions in the suctions observed on the roof due to deviation of the vortex street from the building. One can also observe that the scale of vortices shed from the spoiler is smaller as the orientation angle is lower and zones of positive pressure are developed in the roof leading-edge region when spoilers are utilized. In these zones, high suction pressures are usually observed owing to strong flow separation occurring in building configurations without flow disturbers. On the other, when spoiler orientations with positive angles (counterclockwise direction) are adopted, the scale of the vortices generated by the disturber is also smaller when compared with the vortex scales observed in a building configuration without spoiler, but the vortex street deviation is not as significant as that observed for negative angles. Figure 12 shows the pressure fields obtained around and inside a building model with opening in the upstream wall. This is the most critical situation for the roof structure, considering that high positive pressures may develop internally, while strong negative pressures are observed externally. In this case, the roof structure is submitted to high uplift loading, which is usually considered as the main responsible for structural failures in low-rise buildings, especially during wind storms. The external flow patterns are similar to those identified previously for a building model without opening, where the process of vortex street deviation and its dependency on the spoiler orientation is also observed here. The internal flow field shows a distribution with predominantly positive pressures, where vortices are eventually shed into the internal environment from the top of the opening. Notice that the present flow configuration may also create significant loads on the building walls owing to a positive pressure field developed internally, mainly for zones of external suctions as the leeward and lateral walls.

The time-averaged force coefficient C_z and the distribution of time-averaged pressure over the upstream roof zone are the reference data used here to determine the PID control parameters, considering building configurations with and without opening. From the results obtained in the static analysis, one can elaborate the proportional gain curve k_p (see Fig. 13 for building without opening), where the relative error between the time-averaged force coefficient C_z on the windward roof and the corresponding optimal value (C_{zm} with spoiler at -8°) are presented as functions of the spoiler orientation angle. The bandwidth (P_b) is obtained considering the maximum error amplitude and leads to a first approximation for the gain constant k_p (ratio between the range of angles investigated, -12° to 12°, and the bandwidth obtained), which is a fundamental parameter utilized during the development of the control algorithm.

The spoiler is also submitted to dynamic analyses in order to obtain additional model parameters existing in the PID control equations, where flow disturbances are generated on the roof by small perturbations imposed to the spoiler orientation angle within a small time interval. The dynamic analysis is performed here as follows: after the flow is fully

developed at t = 40 s, the spoiler is allowed to rotate uniformly with angular velocity ω = -0,013963 rad/s, considering an initial orientation at 0° and increasing up to the optimal orientation angle (-8°) after 10 s, approximately, for the building configuration without opening. When the building configuration with opening is considered, this time interval and optimal orientation angle are reduced to 5 s and -4°, respectively (see results obtained during the static analysis). Notice that the angular velocity utilized for spoiler perturbation must be chosen carefully to avoid numerical instabilities.

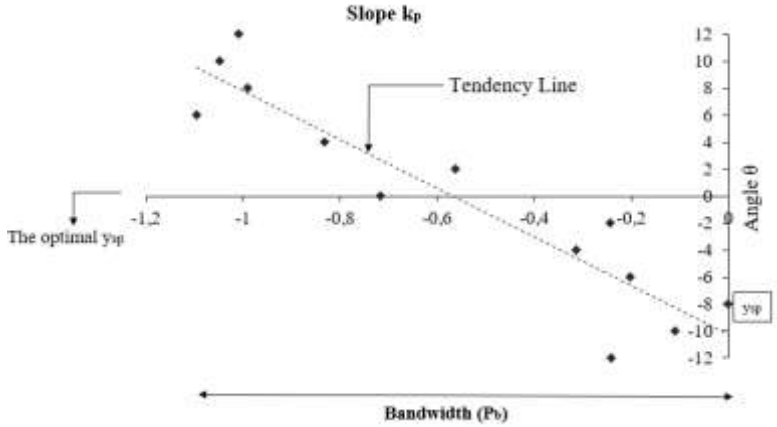

Figure 13: Slope k_p for building configuration without opening.

Time histories of force coefficients evaluated on the windward roof are presented in Fig. 14, considering predictions obtained during the present analysis. Results are compared with force coefficients obtained for building configuration without spoilers, where one can see that a significant reduction in the force coefficients is observed on the windward roof when a flow disturber is considered, and this reduction is improved when a controlled spoiler is utilized. Notice that the force coefficients present time-averaged values very close to the optimum value (at -8°) obtained from the static analysis after t = 70 s, approximately, considering a building configuration without opening. On the other hand, the optimum value is achieved at t = 45 s when a building configuration with opening is considered.

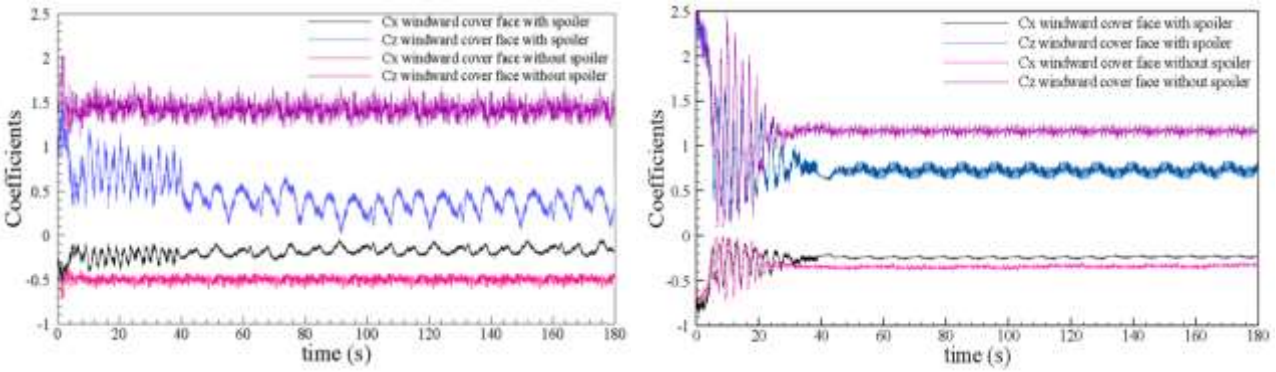

(a) (b)

Figure 14: Time-histories of force coefficients on the windward roof for building configurations with spoilers: (a) building without opening; (b) building with opening.

The PID control parameters obtained from the static and dynamic analyses are presented in Table 7. The sampling period is the time required to modify the spoiler orientation by 0.8°, according to the angular speed utilized here, and the derivative time T_D refers to the time needed to modify the spoiler orientation until the set point (y_{sp}) is obtained. The integral time T_i is the time necessary to achieve stabilization, that is, when the spoiler orientation is oscillating around the optimal angle with maximum displacement amplitude of 2° and minimal angular velocity. According to Hägglund and Åström (1995), parameters obtained from preliminary analyses must be considered as a starting point for model calibration. Nevertheless, the parameters obtained here lead to effective reduction of pressure suction on the roof by the control algorithm, according to the values expected, and no major adjustments are required.

Figure 15 shows results obtained for building configurations without and with an opening in the windward wall of the building model, where controlled spoilers are utilized using the PID control parameters presented in Table 7. Results obtained here are compared with predictions obtained with static spoilers at the ideal orientation angle (θ_{opt} = -8°). Force coefficients are evaluated on the windward roof surface over the time, which clearly demonstrate the influence of the

present control device on the mitigation of flow-induced forces acting on the roof structure. Notice that the control algorithm is activated at t = 40 s, when a significant reduction of force magnitude is observed for both the force components and building configurations analyzed. In addition, one can see that the control scheme adopted here is able to maintain the force coefficients with time-averaged values close to those defined as optimal during the preliminary analyses.

Table 7 PID control parameters.

Parameter	Building without opening	Building with opening
Integral time (T_I)	50 seconds	25 seconds
Derivative time (T_D)	10 seconds	5 seconds
Dimensional coefficient (N)	8	8
Derivative Constant (c)	0.1	0.1
Sampling period (h)	1 second	1 second
Bandwidth (P_b)	1.096	0.912
Set point (y_{sp} = $Cz(\theta = \theta_{opt})$)	0.413 (θ_{opt} = -8°)	0.684 (θ_{opt} = -4°)
Gain constant (k_p)	0.382	0.456
Optimal angle – zero error (θ_{opt})	-8°	-4°

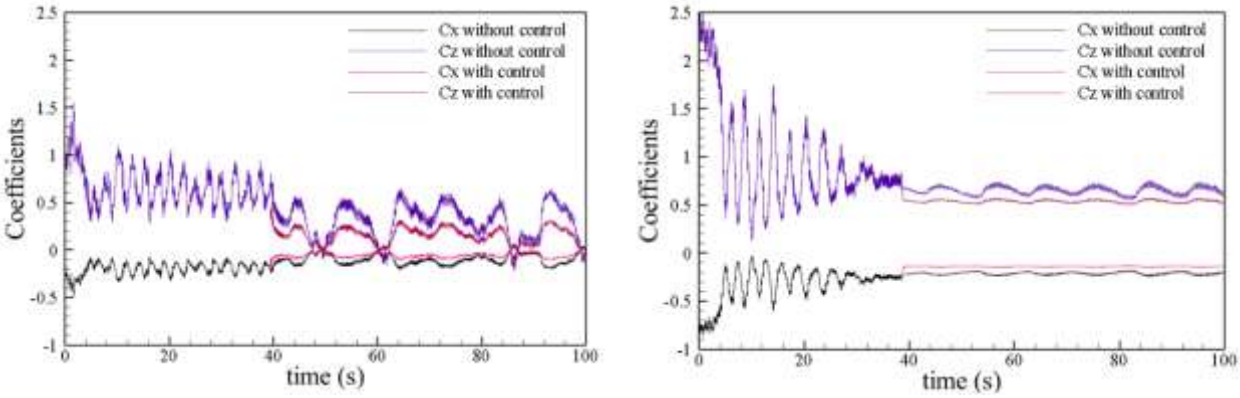

Figure 15: Time histories of force coefficients on the windward roof for building configurations with and without controlled spoilers: (a) building configuration without opening; (b) building configuration with opening.

5.2 Three-dimensional simulations

Numerical simulations are performed in this section taking into account three-dimensional building models based on the experimental investigation carried out by Loredo-Souza (1992). Details on the geometry of the computational domain and boundary conditions adopted here are shown in Fig. 2, while physical and numerical parameters utilized in the present simulations are indicated in Table 1. Notice that a uniform and smooth flow is considered to characterize a specific flow condition used in the wind tunnel simulations.

Mesh information is presented in Table 8 according to the test cases investigated here, including number of finite elements and nodes used in the spatial discretization procedure. The size of the smallest element in the computational mesh and the dimensionless wall distance y^+ are similar to those utilized during the two-dimensional simulations.

Table 8 Cases investigated and the corresponding mesh characteristics.

Test case	Wind direction	Openings	Number of nodes	Number of elements
GP3D01	90°	-	759,350	4,000,507
GP3D02	0°	-	872,702	4,494,335
GP3D03	0°	D	880,296	4,555,942
GP3D04	0°	D, with spoiler	867,915	4,472,596

Three-dimensional models considering the worst building configuration in terms of pressure resultant on the roof and a building configuration with impermeable walls are analyzed. Predictions obtained here are compared with results obtained by Loredo-Souza (1992) experimentally and results obtained from the two-dimensional analyses presented formerly, from which the feasibility of two-dimensional predictions can be evaluated. A building model with an opening

in the front wall and continuous spoilers along the windward and downward roof edges is also analyzed considering the PID control algorithm and parameters obtained from two-dimensional calibration.

The building models *GP3D01* and *GP3D02* are investigated first to evaluate the distribution of external pressures on the building walls, which correspond to three-dimensional equivalents of the test cases *galp01* and *galp02* analyzed earlier (see Table 2 for building configurations and wind directions). In the following analysis, a building model with an opening in the front wall (*GP3D03*) is also investigated (corresponding to the test case *galp03*). The test case *GP3D04* is based on the geometric configuration utilized for the building model *GP3D03*, where spoilers with horizontal orientation are included near the windward and leeward roof edges.

Figure 16 shows predictions obtained here considering the time-averaged pressure coefficients on the walls of the building, where results are visualized using a plan view at $z = 0.05L$, corresponding to 40% of the wall height. The same height was utilized by Loredo-Souza (1992) to position the pressure sensors for experimental evaluation of internal pressure. Results obtained from the wind tunnel experiment and numerical predictions using a two-dimensional approach were presented previously in Figs. 3 and 4, where values recommended by the Brazilian standard NBR6123 (ABNT, 1988) were also indicated. One can observe that the three-dimensional simulations performed here obtained a better approximation to the experimental predictions when the results obtained with the two-dimensional approach are considered comparatively.

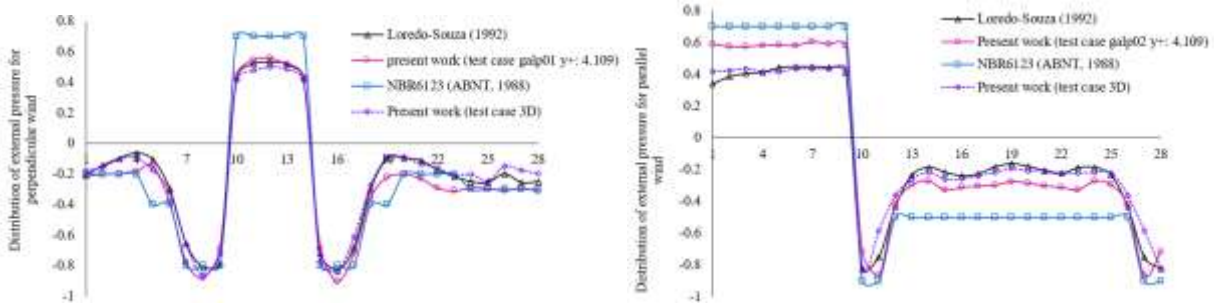

(a) (b)

Figure 16: Mean pressure coefficients on external building walls: (a) angle of wind incidence=90°; (b) angle of wind incidence=0°.

Time-averaged drag and lift coefficients evaluated over the building walls are presented in Table 9 for case GP3D01, where a comparison with results obtained from equivalent building configuration using a two-dimensional approach and a prediction by the Brazilian standard NBR6123 is performed. One can observe that the present two-dimensional simulation was able to reproduce satisfactorily the full model predictions in terms of longitudinal and lateral force coefficients.

Table 9 Time-averaged drag and lift coefficients on the building walls and ventilation rate for two and three-dimensional simulations.

Test cases/reference	C_{DM}	C_{LM}
3D model, wind at 90° (GP3D01)	1.047	-0.019
2D model, wind at 90° (galp01)	1.135	-0.049
NBR 6123	1.000	-

Table 10 shows results related to mean pressure and force coefficients evaluated on the roof of the building models analyzed in this work. Predictions obtained here with three-dimensional models are compared with results from similar building configurations using a two-dimensional approach (B-B section cut) and angle of wind incidence at 0°. It is observed that a good agreement is obtained when results from two and three-dimensional simulations of a given building configuration are compared, indicating that a two-dimensional approach is able to reproduce satisfactorily the aerodynamic forces induced by the wind on building roofs for buildings with geometric characteristics similar to those investigated here.

Figure 17 shows the distribution of time-averaged pressure coefficient over the building roofs considering an intermediate section along the building length. Results obtained here are compared with the classical experimental predictions obtained Chien et al. (1951) using the same flow conditions, but with a slightly different geometric configuration ($H/W = 0.5$; roof pitch = 15°). In addition, numerical predictions with two-dimensional models and spoilers are also presented. One can see that the pressure values on the roof are significantly reduced and the pressure distribution is equalized when the building model with spoilers is utilized, while a good agreement is observed with

respect to the experimental results for the building models with no spoilers included. Chien et al. (1951) also indicate a mean pressure coefficient of -1.35 over the windward roof, which is close to the numerical results obtained here: -1.395 (2D analysis) and -1.327 (3D analysis).

Table 10 Time-averaged pressure and force coefficients on the building roofs for two and three-dimensional simulations.

Test cases	Windward roof			Leeward roof		
	Czm	Cxm	Cpm	Czm	Cxm	Cpm
3D model, wind at 0° (GP3D02)	1.361	-0.475	-1.327	0.850	0.378	-0.865
2D model, wind at 0° (sa0000)	1.454	-0.511	-1.395	0.925	0.325	-0.945
Difference	6.40%	5.12%	7.10%	8.78%	14.02%	9.25%
3D model with opening, wind at 0° (GP3D03)	1.197	-0.464	-1.217	0.953	0.343	-1.113
2D model with opening, wind at 0° (ca0000)	1.220	-0.418	-1.214	1.022	0.356	-1.176
Difference	1.89%	9.91%	2.47%	7.22%	3.85%	5.65%
3D model with spoiler, wind at 0° (GP3D04)	1.931	-0.405	-1.022	2.412	0.396	-1.187
2D model with spoiler, wind at 0° (cash00)	1.953	-0.407	-0.767	2.416	0.513	-1.148
Difference	0.10%	0.50%	24.95%	0.17%	29.55%	3.29%

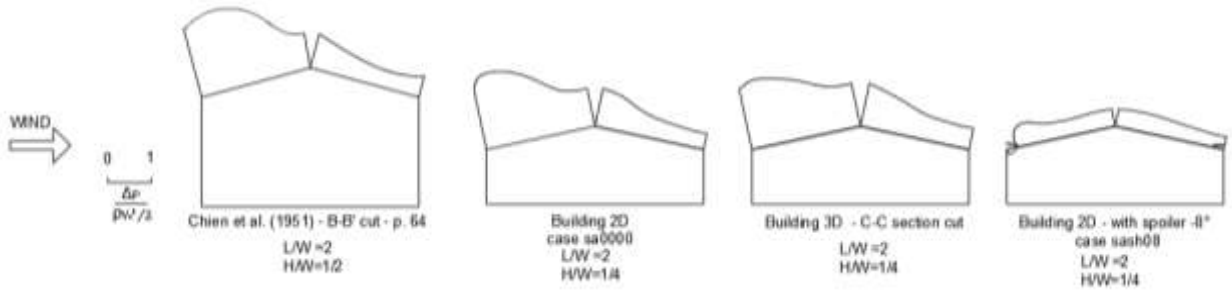

Figure 17: Distributions of time-averaged pressure coefficient Cp over the windward and leeward building roofs.

Pressure distributions on walls and roofs of a building model without openings are shown in Fig. 18 for angles of wind incidence at 0° (test case *GP3D02*) and 90° (test case *GP3D01*). The maximum and minimum values found in any of the cases determine the pressure range analyzed. Notice that high suctions are developed along the roof windward edge and roof ridge for angles of flow incidence equal to 90° and 0°, respectively. On the other hand, positive pressures are observed on the walls exposed directly to the wind.

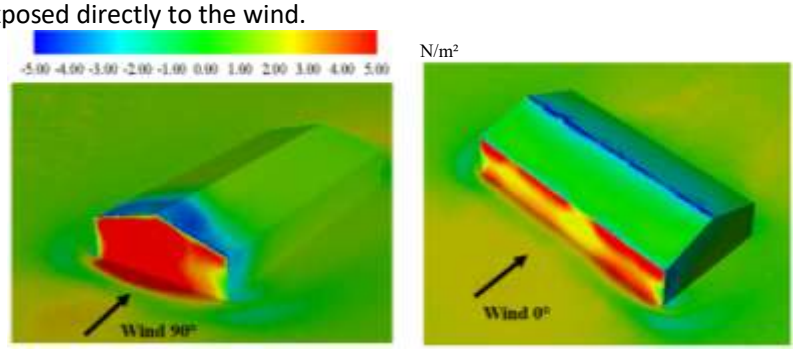

(a) (b)

Figure 18: Pressure fields on walls and roofs for impermeable building model: (a) test case GP3D01; (b) test case GP3D02.

The flow circulation around the building can be visualized in Fig. 19, where time-averaged streamlines obtained from the numerical simulations carried out here are presented for the angles of wind incidence considered in this work. A strong recirculation zone is identified in front of the windward wall of the building for both the flow incidence proposed in the present analysis, which is associated with the development of horseshoe vortices. Flow separation is also observed along the windward roof edges, especially at the roof ridge for wind incidence at 90°, where high suctions occur. The flow is reattached to the roof surface at a short distance downstream the separation zone. When the wind is flowing with an angle of incidence equal to 0°, one can see that flow reattachment is not observed after the flow particles pass the roof ridge, producing suctions on the leeward roof region.

Final simulations are performed to evaluate the influence of a controlled spoiler on the mitigation of aerodynamic loads on the roof structure of the building using three-dimensional models. Taking into account that the comparisons carried out previously considering results obtained with two and three-dimensional models demonstrated a good agreement for equivalent building configurations, the PID control formulation and parameters adopted previously are maintained here. In the present analysis, the flow field is considered to be fully developed at t = 20 s, when the motion of the windward spoiler is activated. The instantaneous orientation of the controlled spoiler is defined according to the PID control algorithm, while the leeward spoiler is kept fixed horizontally. Notice that the control system utilized here is based only on aerodynamic loads evaluated on the windward roof.

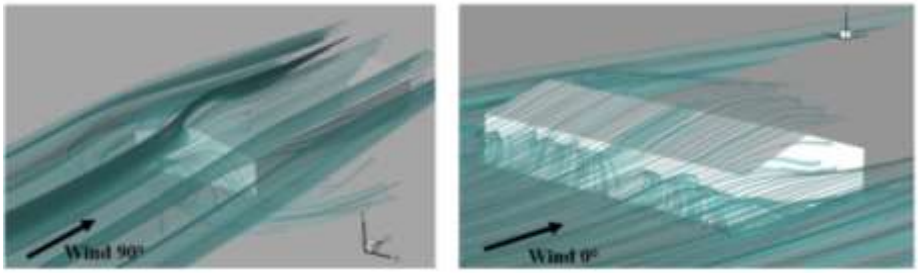

(a) (b)

Figure 19: Time-averaged streamlines for impermeable building model: (a) test case GP3D01; (b) test case GP3D02.

Figure 20 presents results referring to instantaneous streamlines obtained around the building location, where predictions related to the test cases *GP3D03* and *GP3D04* are analyzed comparatively for angle of wind incidence at 0°. The test case *GP3D03* corresponds to a building model with an opening near the right end of the front wall, while the test case *GP3D04* includes spoilers along the windward and leeward edges of the roof. One can see that the windward spoiler generates perturbations in the wake flow above the windward roof region, where the streamlines are deviated upwards when compared with the streamlines obtained using a building model without spoilers, eliminating the suction peaks usually identified along windward roof edges of buildings without flow disturbers.

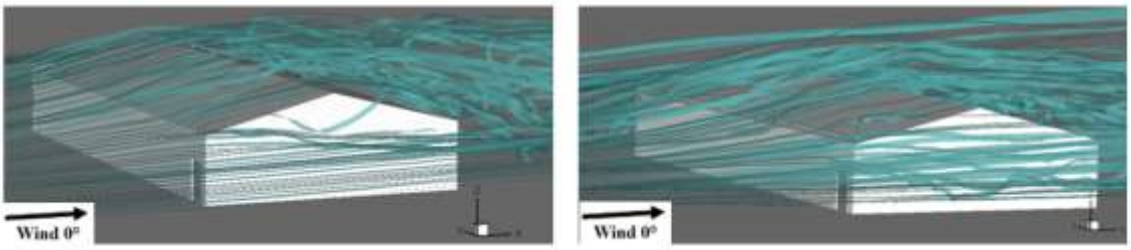

(a) (b)

Figure 20: Instantaneous streamlines around the building location: (a) test case GP3D03; (b) test case GP3D04.

Instantaneous pressure distributions are presented in Fig. 21 considering the test case GP3D04, where a three-dimensional view near the opening location and section cuts along the building longitudinal direction are shown. At this time instant, both the spoilers are still oriented horizontally, when there are significant suction pressures developed on the roof, despite generating an overpressure zone at the windward edge, where there was suction previously. In both sections, one can see that the roof ridge is strongly affected by large pressure suctions, although these suctions are significantly reduced later owing to the motion of the windward spoiler, which deviates the vortex street from the roof surface to a higher level.

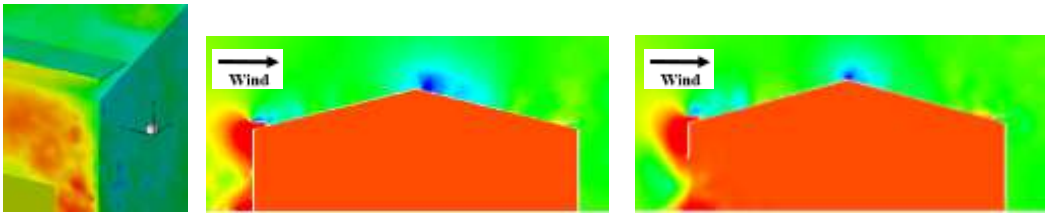

(a) (b) (c)

Figure 21: Instantaneous pressure fields at t = 20 s, test case *GP3D04*: (a) three-dimensional view near the opening location; (b) section cut at y = 0.045L; (c) section cut at y = -0.045L.

Figure 22 shows time histories of the force coefficients evaluated on the windward roof taking into account a building configuration corresponding to the test case *GP3D04*, where an opening in the windward wall and spoilers along the windward and leeward roof edges are considered. The motion of the windward spoiler is activated at t = 20 s using the PID control algorithm developed previously. One can see that after the time instant t = 20 s, a significant reduction in the magnitude of the force coefficients is observed, with well-defined time average and amplitude over the remaining simulation time. A very stable process is obtained, where the optimal angle and optimal force coefficient values are achieved quickly, with the spoiler orientation oscillating within the angle interval [-4°, -6°]. Table 11 summarizes the results obtained here using two and three-dimensional models for a building configuration with opening and controlled spoiler. One can see that the agreement between the two and three-dimensional approaches is very good in general, although a lower lift force is obtained with the three-dimensional model after the control spoiler is activated. Time-averaged and standard deviation values obtained in this work for the *Cz* and *Cx* forces coefficients on the windward roof (at t > 20 s) are 0.524 and 0.304, -0.185 and 0.106, respectively, for a building configuration corresponding to the test case *GP3D04* and controlled spoiler.

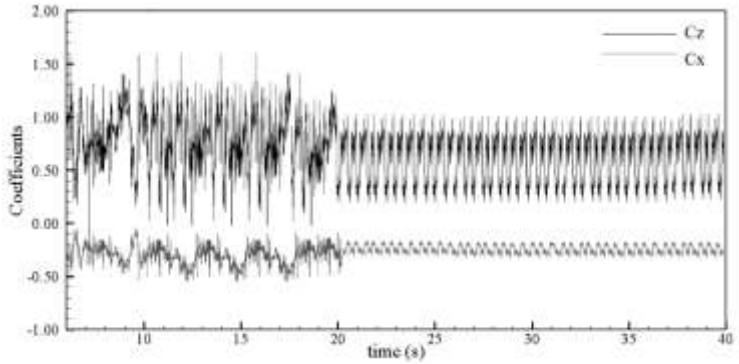

Figure 22: Time histories of force coefficients on the windward roof, test case GP3D04.

Table 11 Two and three-dimensional results for building configuration with opening and controlled spoiler.

Parameter	Two-dimensional analysis	Three-dimensional analysis
Optimal angle	-4°	-4° to -6°
C_{zm} (t < 20 s)	0.800	0.772
C_{zm} ($t \geq$ 20 s)	0.613	0.524
C_{xm} (t < 20 s)	-0.268	-0.267
C_{xm} ($t \geq$ 20 s)	-0.198	-0.185
Stabilization time after control	10 s	5 s

Instantaneous pressure fields are presented in Fig. 23 using section cuts defined at y = -0.45L, where the influence of the spoiler motion on the roof loading can be better evaluated. Results related to the test cases *GP3D03* and *GP3D04* are analyzed comparatively considering flow patterns obtained before and during the action of the PID control. One can observe that high pressure suctions are developed on the building roof when no mitigation device is utilized, especially at the ridge and windward edge. However, these high suction zones are significantly reduced when a windward spoiler is simply introduced to the building configuration with horizontal orientation and no motion. The pressure mitigation is improved when a controlled spoiler is utilized, where the high suction zones are eliminated and the vortex street is deviated from the roof surface.

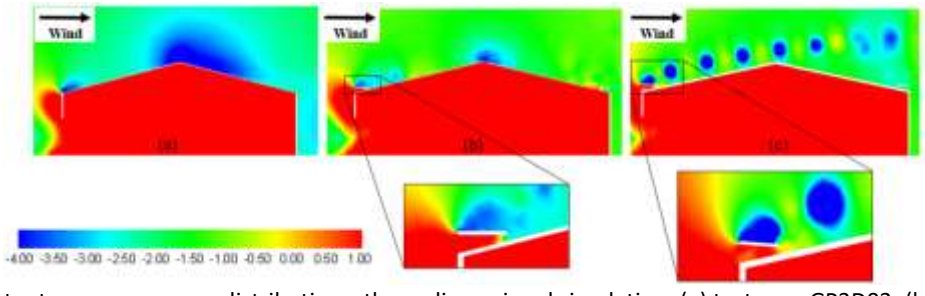

Figure 23: Instantaneous pressure distributions, three-dimensional simulation: (a) test case GP3D03; (b) test case GPD304 before PID control; (c) test case GPD304 during PID control.

6 CONCLUSIONS

A numerical investigation was proposed in this work to evaluate the influence of controlled spoilers on pressure mitigation over low-rise building roofs using PID control. A building model analyzed experimentally by Loredo-Souza (1992) was utilized to validate the present formulation, where two and three-dimensional simulations were performed considering several building configurations and different directions of wind incidence. A two-dimensional approach was initially adopted to verify the numerical formulation and computational meshes using the wind tunnel predictions referring to external pressure on building walls and internal pressure for building configurations with openings. A good agreement was observed between the experimental predictions and two-dimensional results obtained here. In addition, the control scheme was calibrated employing static and dynamic analyses based on a section cut of the three-dimensional model, where spoilers were included along the windward and leeward roof edges. The control algorithm was formulated considering only wind-induced loads on the windward roof, since the pressure distribution on the leeward roof is not significantly altered by the spoiler orientation. From preliminary tests with a two-dimensional building it was observed that spoilers with clockwise orientation angles obtained significant reductions of aerodynamic loads on roof surfaces, by dissipating high pressure suctions at the roof ridge and windward edge, while deviating upwards the vortices shed from the spoiler. Although building configurations with opening in the windward wall led to expressive uplift forces on the roof, significant load reductions were also observed when spoilers were utilized. Optimal spoiler orientations of -8° and -4° were determined for building models without and with opening in the front wall, respectively, although all the orientation angles evaluated here obtained some level of pressure mitigation, especially when building configurations with opening were adopted. Building configurations with controlled spoilers were simulated and results demonstrated that the control formulation proposed here was able to reduce the wind-induced loads on the building roofs to the desired limits, considering parameters obtained from model calibration and instantaneous flow conditions. After the control mechanism is activated, the spoiler orientation changes slightly around the optimal angle, presenting angular displacements of small amplitude, while the aerodynamic forces on the roof show a very stable response over the time. Three-dimensional simulations were finally carried out and results compared with experimental predictions obtained from wind tunnel modeling, where a good agreement was observed. Comparisons with two-dimensional results obtained previously were also performed, which demonstrated that a two-dimensional approach can provide good approximations to the problem investigated here.

Author's Contribuitions: Conceptualization, Investigation and Writing GP Bianchin; Supervision, AL Braun.

Editor: Marco L. Bittencourt

Acknowledgements: The authors would like to thank the National Council for Scientific and Technological Development (CNPq, Brazil) and the Brazilian Federal Agency for Support and Evaluation of Graduate Education (CAPES, Brazil) for the financial support. The present research was developed using computational resources provided by the High Performance Computing Center (NACAD/UFRJ, Brazil) and the National Center for High Performance Computing (CENAPAD/UNICAMP, Brazil).

References

J. Blessmann, Ação do Vento em Telhados, 2ª ed., Editora UFRGS, Porto Alegre, 2009.

G. Li, S. Gan, H. Li, Wind pressure mitigation on gable roofs for low-rise buildings using spoilers, Journal of Structural Engineering – ASCE 144(8) (2018) 1–14. https://doi.org/10.1061/(ASCE)ST.1943-541X.0002103

J.D. Holmes, Wind Loading of Structures, 3rd ed., Taylor & Francis, Boca Raton, 2015.

D. Banks, The Suction Induced by Conical Vortices on Low Rise Buildings with Flat Roofs, Ph.D. dissertation, Colorado State University, 2000.

D. Prasad, T. Uliate, M.R. Ahmed, Wind loads on low-rise building models with different roof configurations, International Journal of Fluid Mechanics Research 36(3) (2009) 231–243. https:// doi.org/10.1615/InterJFluidMechRes.v36.i3.30

P. Huang, X. Peng, M. Gu, Aerodynamic devices to mitigate rooftop suctions on a gable roof building, Journal of Wind Engineering and Industrial Aerodynamics 135 (2014) 90–104. https://doi.org/10.1016/j.jweia.2014.10.015

J. Blessmann, Pressão Interna, 3ª ed., Editora UFRGS, Porto Alegre, 2013.

D. Surry, J.X. Lin, The effect of surroundings and roof corner geometric modifications on roof pressures on low-rise buildings, Journal of Wind Engineering and Industrial Aerodynamics 58 (1995) 113–138. https://doi.org/10.1016/0167-6105(95)00016-K

G.A. Kopp, C. Mans, D. Surry, Wind effects of parapets on low buildings: Part4. Mitigation of corner loads with alternative geometries, Journal of Wind Engineering and Industrial Aerodynamics 93 (2005) 873–888. https://doi.org/10.1016/j.jweia.2005.08.004

G. Bitsuamlak, W. Warsido, E. Ledesma, A. Chowdhury, Aerodynamic mitigation of roof and wall corner suctions using simple architectural elements. Journal of Engineering Mechanics – ASCE 139(3) (2013) 396–408. https://doi.org/10.1061/(ASCE)EM.1943-7889.0000505

M.A. Mooneghi, R. Kargarmoakhar, Aerodynamic mitigation and shape optimization of buildings: review, Journal of Building Engineering 6 (2016) 225-235. https://doi.org/10.1016/j.jobe.2016.01.009

A.P. Robertson, Effect of eaves detail on wind pressures over an industrial building, Journal of Wind Engineering and Industrial Aerodynamics 38 (1991) 325–333. https://doi.org/10.1016/0167-6105(91)90051-W

A-M. Aly, J. Bresowar, Aerodynamic mitigation of wind-induced uplift forces on low-rise buildings: a comparative study, Journal of Building Engineering 5 (2016) 267–276. https://doi.org/10.1016/j.jobe.2016.01.007

[a]G.W. Alminhana, A.L. Braun, A.M. Loredo-Souza, A numerical study on the aerodynamic performance of building cross-sections using corner modifications, Latin American Journal of Solids and Structures 15(7) (2018) 1–18. https://doi.org/10.1590/1679-78254871

[b]G.W. Alminhana, A.L. Braun, A.M. Loredo-Souza, A numerical-experimental investigation on the aerodynamic performance of CAARC building models with geometric modifications, Journal of Wind Engineering and Industrial Aerodynamics 180 (2018) 34–48. https://doi.org/10.1016/j.jweia.2018.07.001

A. Kareem, T. Kijewski, Y. Tamura, Mitigation of motions of tall buildings with specific examples of recent applications, Wind and Structures 2(3) (1999) 201–251. https://doi.org/10.12989/was.1999.2.3.201

A. Baskaran, T. Stathopoulos, Roof corner wind loads and parapet configurations, Journal of Wind Engineering and Industrial Aerodynamics, 29 (1988) 79–88. https://doi.org/10.1016/0167-6105(88)90147-X

F. Wu, Full-scale study of conical vortices and their effects near corners, Texas Tech University. Lubbock, Texas, 2000. http://hdl.handle.net/2346/12213

S. Pindado, J. Meseguer, Wind tunnel study on the influence of different parapets on the roof pressure distribution of low-rise buildings, Journal of Wind Engineering and Industrial Aerodynamics 91 (2003) 1133–1139. https://doi.org/10.1016/S0167-6105(03)00055-2

W. Suaris, P. Irwin, Effect of roof-edge parapets on mitigating extreme roof suctions, Journal of Wind Engineering and Industrial Aerodynamics 98 (2010) 483–491. https://doi.org/10.1016/j.jweia.2010.03.001

D. Banks, R.N. Meroney, P.P. Sarkar, Z. Zhao, F. Wu, Flow visualization of conical vortices on flat roofs with simultaneous surface pressure measurement, Journal of Wind Engineering and Industrial Aerodynamics 84 (2000) 65–85. https://doi.org/10.1016/S0167-6105(99)00044-6

L.A Sangalli, A.L. Braun, A fluid-structure interaction model for numerical simulation of bridge flutter using sectional models with active control devices. Preliminary results, Journal of Sound and Vibration 477 (2020) 1–33. https://doi.org/10.1016/j.jsv.2020.115338

K.J. Aström, T. Hägglund, PID Controllers, 2nd ed., Instrument Society of America, Research Triangle Park-NC 1995.

K.J. Aström, T. Hägglund, Advanced PID Control, Instrument Society of America, Research Triangle Park-NC 2005.

[a]A.L. Braun, A.M. Awruch, Aerodynamic and aeroelastic analyses on the CAARC standard tall building model using numerical simulation, Computers and Structures 87(9-10) (2009) 564-581. https://doi.org/10.1016/j.compstruc.2009.02.002

F.M. White, Viscous Fluid Flow, 3rd ed., McGraw-Hill, New York, 2005.

J. Smagorinsky, General circulation experiments with the primitive equations, I, the basic experiment, Monthly Weather Review 91 (1963) 99-135. https://doi.org/10.1175/1520-0493(1963)091<0099:GCEWTP>2.3.CO;2

M. Germano, U. Piomelli, P. Moin, W.H. Cabot, A dynamic subgrid-scale eddy viscosity model, Physics of Fluids 3 (1991) 1760-1765. https://doi.org/10.1063/1.857955

D.K. Lilly, A proposed modification of the Germano subgrid-scale closure method, Physics of Fluids 4 (1992) 633-635. https://doi.org/10.1063/1.858280

T.T. Soong, Active Structural Control: Theory and Practice, Longman Scientific and technical, Essex, UK, 1990.

K. Ogata, Modern Control Engineering, 5th ed., Pearson Prentice Hall, New York, 2010.

A.J. Chorin, Numerical solution of Navier-Stokes equations, Mathematics of Computation 22 (1968) 745 –762. https://doi.org/10.1090/S0025-5718-1968-0242392-2

O.C. Zienkiewicz, R.L. Taylor, P. Nithiarasu, The Finite Element Method for Fluid Dynamics, 7th ed., Butterworth-Heinemann, Waltham, 2013.

P. Nithiarasu, R.W. Lewis, K.N. Seetharamu, Fundamentals of the Finite Element Method for Heat and Mass Transfer, 2nd ed., Wiley, Chichester, West Sussex, 2016

P.D. Thomas, C.K. Lombard, Geometric conservation law and its application to flow computations on moving grids. AIAA Jl 17, 1030 (1979). https://doi.org/10.2514/3.61273

M. Lesoinne, C. Farhat, Geometric conservation laws for flow problems with moving boundaries and deformable meshes, and their impact on aeroelastic computations, Computer Methods in Applied Mechanics and Engineering, 134(1-2) (1996) 71-90. https://doi.org/10.1016/0045-7825(96)01028-6

A.L. Braun, A.M. Awruch, Finite element simulation of the wind action over bridge sectional models: application to the Guamá River Bridge (Pará State, Brazil), Finite Elements in Analysis and Design 44(3) (2008) 105-122. https://doi.org/10.1016/j.finel.2007.11.006

[b]A.L. Braun, A.M. Awruch, A partitioned model for fluid-structure interaction problems using hexahedral finite elements with one-point quadrature, International Journal for Numerical Methods in Engineering 79(5) (2009) 505-549. https://doi.org/10.1002/nme.2566

A.M. Loredo-Souza. Influence of opening type on mean internal pressures in low buildings. In: Proceedings of the Ninth International Conference on Wind Engineering, New Delhi (1995) 1151-1161.

A.M. Loredo-Souza. Influência do tipo de abertura e das características do vento simulado na pressão interna em um pavilhão industrial. Porto Alegre: UFRGS, 1992. Dissertação (Mestrado) – Programa de Pós-Graduação em Engenharia Civil, Universidade Federal do Rio Grande do Sul, Porto Alegre, 1992

L. Bruno, S. Khris. The validity of 2D numerical simulations of vertical structures around a bridge deck, Math. Comput. Model, vol. 37, pp.795-828, 2003.

ABNT, NBR6123 – Forças Devidas ao Vento em Edificações, Associação Brasileira de Normas Técnicas, Rio de Janeiro, 1988.

N. Chien, Y. Feng, H.-J. Wang, T.-T. Siao, Wind-tunnel studies of pressure distribution on elementary building forms, Air Infiltration and Ventilation Centre (1951) 2-117.